PIC Simulation of SPT Hall Thrusters: High Power Operation and Wall Effects

by

Kay Ueda Sullivan

Submitted to the Department of Aeronautical and Astronautical Engineering
in partial fulfillment of the requirements for the degree of

Master of Science in Aeronautical and Astronautical Engineering

at the

MASSACHUSETTS INSTITUTE OF TECHNOLOGY

June 2004

© Massachusetts Institute of Technology 2004. All rights reserved.

Author ....
Department of Aeronautical and Astronautical Engineering
May 14, 2004

Certified by ....
Manuel Martinez-Sanchez
Professor
Thesis Supervisor

Certified by ....
Oleg Batishchev
Research Scientist
Thesis Supervisor

Accepted by ....
Edward M. Greitzer
H.N. Slater Professor of Aeronautics and Astronautics
Chair, Committee on Graduate Students

MASSACHUSETTS INSTITUTE OF TECHNOLOGY
JUL 0 1 2004
LIBRARIES

AERO

PIC Simulation of SPT Hall Thrusters: High Power Operation and Wall Effects

by

Kay Ueda Sullivan

Submitted to the Department of Aeronautical and Astronautical Engineering
on May 14, 2004, in partial fulfillment of the
requirements for the degree of
Master of Science in Aeronautical and Astronautical Engineering

Abstract

The fully kinetic Hall Thruster simulation built by [1] and used by [2] is further refined and used to obtain results for the P5 SPT Hall thruster at 3kw and 5kw operation. Performance data agree well with experiments [3], although very low values of anomalous diffusivity must be used for convergence. Particle temperatures and plasma potentials in the chamber are similar to experimental results, although charged particles and peak ionization rates are found further upstream than is observed experimentally. Electron transport mechanisms and the magnetic field configuration are analyzed for their physical consistency and effect on particle placement. Electron mobility rates are found to be physical although the reason for high Hall parameter is still unclear. Strong magnetic mirror effects, that are not reported in experimental data, are found in the simulation. Meanwhile, two sputtering models are added to the simulation and tested. A yield model based on [4]'s theories and implemented with [5]'s functions is found to agree well with experimental yield data for 300eV to 1000eV sources, but produces small yields at thruster operating conditions.

Thesis Supervisor: Manuel Martinez-Sanchez
Title: Professor

Thesis Supervisor: Oleg Batishchev
Title: Research Scientist

Acknowledgments

Thank you Jorge, Shannon, and Paulo for putting up with me these last two years. Some days the office antics are all that keep me sane. A very special thank you to Justin for agreeing to take on the project. May the force be with you. And of course, all of this would have been completely impossible without my advisors. This thesis is brought to you by Dr. Pepper.

Contents

1 **Introduction** **15**

- 1.1 Hall Thrusters 15
- 1.2 Project Objectives 16
- 1.3 A Brief History of Code Development 16
- 1.4 Outline of Research 17

2 **PIC Code Structure** **19**

- 2.1 Basic Structure 19
  - 2.1.1 Particle Motion 19
  - 2.1.2 Poisson Solver 20
  - 2.1.3 Magnetic Field 20
  - 2.1.4 Numerical Tricks 21
  - 2.1.5 Wall Sheath Fix 21
  - 2.1.6 Cathode Model 22
- 2.2 Anomalous Diffusion 23
- 2.3 P5 Geometry 23

3 **P5 Results** **25**

- 3.1 Conditions for Current Runs 25
- 3.2 Simulation Results 25
- 3.3 Effect of Increased Voltage 29
- 3.4 Evolution of density and temperature 30
- 3.5 Discussion 31

4 Electron Transport 41
4.1 Anomalous Diffusion 41
4.2 Isolated Mobility Tests 43
4.3 Wall Effects in the Full Simulation 44
4.3.1 Results 45
4.3.2 Results with Radial B Only 46
4.4 Discussion 51

5 Examining the Magnetic Field 53
5.1 Magnetic Mirroring 53
5.2 Simplified Magnetic Field 53
5.3 New Magnetic Field 55
5.4 Results without Magnetic Screens 56
5.5 Discussion 59

6 Sputtering 61
6.1 Introduction 61
6.2 Simple Model 61
6.3 Yamamura Model 62
6.3.1 Yamamura Normalized Angular Yield 63
6.3.2 Yamamura Normal Yield 64
6.3.3 Low Energy Approximation 64
6.3.4 Neutral Ejection Velocity 65
6.4 Model Validation 66
6.5 Full Simulation Sputtering Results 67
6.6 Discussion 68

7 Conclusions and Future Work 73
7.1 Future Work 74

A Effect of SEE on Classical Collisions 81

List of Figures

2-1 P5 Grid 24

3-1 Radial Magnetic Field used at MIT 26
3-2 Experimental Plasma Potential 3kw [3] 27
3-3 Average Plasma Potential 3kw (left) and 5kw (right) 27
3-4 Experimental Ion Density 3kw [3] 28
3-5 Average Ion Density 3kw (left) and 5kw (right) 28
3-6 Average Neutral to Single Ionization Rate 3kW 29
3-7 Average Xe++ Distribution 3kw (left) and 5kw (right) 29
3-8 Experimental Electron Temperature 3kw [3] 30
3-9 Average Electron Temperature 3kw (left) and 5kw (right) 30
3-10 Rising Ion Density 5kw 32
3-11 Maximum Ion Density 5kw 33
3-12 Falling Ion Density 5kw 34
3-13 Minimum Ion Density 5kw 35
3-14 Rising Electron Temperature 5kw 36
3-15 Maximum Electron Temperature 5kw 37
3-16 Falling Electron Temperature 5kw 38
3-17 Minimum Electron Temperature 5kw 39

4-1 Anode Current versus Time for Various Hall Parameters. 43
4-2 Primary to Secondary Electron Trajectory, inverted electric field . . . 44

4-3 Summary of Electron Cross-Field Velocity. Tested indicates average simulated axial electron velocity. Calculated velocities are from $\mu_{tot} = \frac{e\sum\nu}{m_e\omega_c^2}$, using simulated collision frequencies and field strengths. 45
4-4 Average Electron Temperature with No SEE (left) full $\beta' = 200$ run (right) 46
4-5 Average Electron Density with No SEE (left) full $\beta' = 200$ run (right) 47
4-6 Average Plasma Potential with No SEE (left) full $\beta' = 200$ run (right) 47
4-7 Average Charge with No SEE (left) full $\beta' = 200$ run (right) 48
4-8 Comparing anode current with and without SEE 49
4-9 Ratio of μ_{actual} to μ_{total} 49

5-1 Simplified Radial Magnetic Field 54
5-2 Br only average electron density 55
5-3 Br only average plasma potential in the channel 55
5-4 Br only average electron temperature 56
5-5 Radial Magnetic Field from Koo 57
5-6 P5 Radial Magnetic Field without Magnetic Screens 57
5-7 Anode Current for different magnetic field inputs. P5 clean refers to magnetic field without magnetic screens. 58
5-8 Magnetic field without magnetic screens results - average electron density 59
5-9 Magnetic field without magnetic screens results - average plasma potential in the chamber 59

6-1 Yield Curve for Simple Sputtering Model 67
6-2 Yamamura Model Elemental Results Compared to Garnier Data 350V (top) 500V (bottom) 69
6-3 Yamamura Model Compound Results Compared to Garnier Data 350V (top) 500V (bottom) 70
6-4 Comparing Yamamura and Simple Model to Simulated Yields 71

A-1 Neutral to Single Ionization Rate with $\beta' = 200$(left)$\beta' = 200$ noSEE (right) 82
A-2 Neutral to Double Ionization Rate with $\beta' = 200$(left)$\beta' = 200$ noSEE (right) 82
A-3 Single to Double Ionization Rate with $\beta' = 200$(left)$\beta' = 200$ noSEE (right) 83
A-4 Excitation Rate with $\beta' = 200$(left)$\beta' = 200$ noSEE (right) 83

List of Tables

3.1 Summary of Code and Experimental Thruster Performance 26

4.1 Theoretical Bohm and Actual Mobility Averaged over Grid Region ($\frac{m/s}{V/m}$) 50

4.2 Theoretical Bohm and Actual Mobility Averaged over Grid Region no SEE ($\frac{m/s}{V/m}$) 50

6.1 Parameters Used in Yamamura Equations 65

Chapter 1

Introduction

1.1 Hall Thrusters

Hall thrusters are a type of electrostatic rocket engine characterized by the use of appropriate electric and magnetic fields to accelerate ions from a low density plasma while trapping the electrons with the ExB force. In brief, electrons are emitted by an external cathode and drift azimuthaly around an annular discharge chamber while slowly diffusing toward the anode. A low density gas, usually Xenon, is pumped into the chamber from the anode and ionized by the circulating electrons. The resulting ions, which are not magnetized due to their higher mass, are accelerated by the axial electric field to produce thrust.

Hall thrusters are low thrust engines, less than 1N, and have typically been used for station keeping in Earth orbit. Consequently most current designs are optimized for specific impulses between 1500 and 2000s. There is interest in developing Hall thrusters that will operate efficiently at higher specific impulses, particularly for use in interplanetary missions. Hall thrusters may show more durability and are less complicated mechanically than the gridded Ion engines that currently fill the 3000 to 4000s niche. The key, however, is efficiency and lifetime. Unlike chemical propulsion, the exhaust speed and specific impulse possible in electrostatic thrusters is theoretically limited only by the speed of light and the size of the power plant. In practice, however, the degradation of thruster components through heating and erosion limits the lifetime of high power Hall thrusters.

1.2 Project Objectives

While Hall thrusters have been used in orbit for decades, a detailed understanding of their internal physics is still developing. Computer simulation is proving to be an important tool in this research area. Simulations are able to model regions of the plasma that are difficult to probe experimentally, and a simulated thruster is cheaper to redesign. Under funding from NASA, we are developing a full particle-in-cell simulation of SPT and TAL Hall thrusters. When complete, the developed simulations will serve as both a research tool and a design aid.

1.3 A Brief History of Code Development

The simulation used in this research was built by James Szabo, using the mini-TAL Hall thruster geometry to test the initial model. Szabo obtained performance results that were within 30% of the mini-TAL's experimental performance, and he was able to redesign the thruster numerically to increase thrust and efficiency. Most of the code features described in chapter 2 remain unchanged from what is presented in [1].

Vincent Blateau used the simulation to identify the effect of increased anode voltage on the mini-TAL's efficiency. He later made several modifications to the code, notably to the Poisson solver, cathode model, sheath calculation, and diffusions model, with hopes of successfully modelling the P5, an SPT Hall thruster [2]. Blateau was able to obtain convergence and reasonable performance data only with very low diffusivity, although the internal densities, temperatures, and ionization strengths still differed significantly from experiments.

1.4 Outline of Research

Starting where [2] left off, this research attempts to more accurately simulate the P5 SPT Hall Thruster, validate the existing physical models, and introduce a sputtering model for eventual use in lifetime estimations. Better P5 results, presented in chapter 3, are obtained after returning to Szabo's anomalous diffusion model with a slightly reduced Hall parameter. Chapter 4 goes into more detail on the anomalous diffusions changes as well as presenting an analysis of the entire electron transport mechanism of the simulated P5. Chapter 5 reports the discovery of strong magnetic bottling in the supplied magnetic field, and the effects of changing the magnetic field on the P5 simulation. Finally, chapter 6 describes the two sputtering models added to the code and some preliminary results from both models.

Chapter 2

PIC Code Structure

2.1 Basic Structure

This simulation is a fully particle-in-cell simulation; electrons, ions, and neutrals are all represented as particles. Three dimensions of velocity and two of position are modelled. The thruster is axisymmetric, therefore azimuthal motion is projected back into the radial-axial (z-r) plane. The simulation region is a 2D slice of the thruster starting at the centerline and encompassing the chamber and part of the plume. The cathode is not directly simulated.

2.1.1 Particle Motion

Electrons and ions are moved each iteration using a leapfrog method. The charged particles are moved a half time step in the electric field, then a full time step in the magnetic field, and then another half time step in the electric field. The time step is approximately one third of the electron plasma time or one third of the electron gyro time, whichever is smaller.

After the electromagnetic motion is calculated, collisions are applied. First and second ionization of neutrals, electron-neutral scattering, electron-neutral excitation, ion-neutral scattering, ion-neutral charge exchange, second ionization of ions, and anomalous electron collisions are modelled. The anomalous collisions are used to model the additional Bohm diffusion observed in plasmas. Coulomb collisions were tested in the original model, but were found to have negligible effects and were turned off [1].

The probability of a collision is determined by an exponential decay model. The probability of a particle with collision frequency ν undergoing at least one collision in time dt is $P = 1 - e^{\nu dt}$. A collision event occurs if a random number is less than the probability of a collision. The collisions frequency is calculated using the collision cross-section, the fast particle's velocity, and the slow particle density interpolated to the fast particle's location. If a collision occurs, a second random number is compared to each type of collisions frequency, ionization, scattering, etc., to determine which type of collision is implemented.

2.1.2 Poisson Solver

The electric potential is found by solving Poisson's equation, $\nabla^2\phi = \rho/\varepsilon_0$, on a control volume around each grid node. Due to the higher mesh distortion in the P5, Blateau modified the solving algorithm to use an 8-sided polygon about each node as the control volume cross-section [2]. The TAL model used only a 4-sided polygon. The field is solved for the whole grid by using an iterative Successive-Over-Relaxation technique on the above conditions. At some boundary nodes the full set of equations do not need to be solved. At the anode the potential is the anode voltage. On the free space boundary, the potential is set to -10V or the normal electric field is set to zero, whichever results in the less negative potential. At the dielectric walls, the internal electric field normal to the wall is neglected.

2.1.3 Magnetic Field

Because the self-induced magnetic field is negligible compared to the applied field from a Hall thruster's coils, the simulation uses only a constant magnetic field. This field is precompiled using a Maxwell-type generator and interpolated to the simulation grid upon startup.

2.1.4 Numerical Tricks

To speed up the code, which in a true simulation would suffer from extreme stiffness due to the very fast electron time scale, three numerical tricks are used. First, superparticles are modelled instead of real particles. Each charged particle in the simulation actually represents N real ions or electrons. Simulated neutrals have variable sizes greater than or equal to one superparticle to account for the much higher neutral densities in the chamber. The superparticle size N is determined by the desired number of particles per cell, which is in turn based on computation time and statistics.

Second, the time and length scales of electromagnetic phenomena are modified by introducing an artificial permittivity γ. The artificial permittivity decreases the plasma frequency and increases the Debye length. However, the Debye length must remain smaller than about half the chamber for electromagnetic effects to occur on relatively the correct scale, and once the plasma time drops below the cyclotron time, no added benefit is gained.

Third, the heavy particle mass is reduced by a factor $f = \frac{Mxe_{real}}{Mxe_{simulated}} > 1$. This increases the velocities of the heavy particles by $\sqrt{f}$, allowing ions to exit the simulation region in fewer time steps. In order to maintain the ion density and energy fluxes at their nominal values, the neutral mass flow, the ionization current, and collision cross-sections with heavy particles are also increased by $\sqrt{f}$.

2.1.5 Wall Sheath Fix

The sheath is determined self-consistently by accumulating the charges from impacting ion and electrons. Due to their higher-than-normal velocity but normal density, the ion number fluxes to the walls will be too high by $\sqrt{f}$. This causes the sheath to weaken, and more low energy electrons are lost to the wall than in the actual thruster. Blateau identified that this energy loss was not important in the short-chambered TAL, but became a significant source of error in the P5 geometry [2]. He compensates for the weakened sheath by implementing a logical sheath. The difference between the theoretical and actual sheath magnitudes is computed. Any electron at the dielectric with energy less than $-eK(\Delta\phi^{real} - \Delta\phi^{comp})$ is specularly reflected instead of being accommodated to the wall, where

$$\begin{aligned}\Delta\phi^{real} &= -\frac{kT_e}{e}\ln(0.654\sqrt{\frac{T_e+T_i}{T_e}\frac{m_i}{m_e}}) \qquad (2.1)\\ &\simeq -6.57\frac{kT_e}{e} \qquad (2.2)\end{aligned}$$

and

$$\begin{aligned}\Delta\phi^{comp} &= -\frac{kT_e}{e}\ln(0.654\sqrt{\frac{T_e+T_i}{T_e}\frac{1}{f}\frac{m_i}{m_e}}) \qquad (2.3)\\ &\simeq (-6.57+\frac{1}{2}\ln(f))\frac{kT_e}{e} \qquad (2.4)\end{aligned}$$

To maintain the current balance to the wall, an electron with $E > \Delta\phi^{real}$ in the vicinity of the wall impact is chosen to impact on the wall instead. This reflects the fact that in the actual plasma, only these high energy electrons can reach the wall, while in the computational plasma, with its weaker sheath, lower energy electrons can also reach the wall.

If at the end of an iteration there are not enough high energy electrons to match all wall collisions, the coefficient K is multiplied by 0.95 and the remaining collisions are "forgotten". The lack of high energy electrons indicates that the estimated sheath is too strong. The coefficient K serves to reduce the analytical sheath strength.

2.1.6 Cathode Model

The cathode is not included in the simulation region, therefore fluxes through the free space boundary must account for the injected electrons. The current cathode model was developed by Blateau [2]. Neutrality is maintained along the free space boundary by injecting electrons with a half-Maxwellian distribution in cells with positive potential. Boundary cells with negative potential are left alone. Electrons hitting the upper free space boundary are reflected with an energy loss to simulate collisions with the walls at the end of the magnetic field lines.

2.2 Anomalous Diffusion

In [6], Blateau used a direct random walk method for simulating anomalous diffusion. As reported there, the simulation only converged for very low values of diffusion. Performance characteristics for that case were within 15% of experimental data, but the electron temperature, in particular, was surprisingly high. A 2D test of the diffusion model, however, showed that it was not producing mobility, and that it artificially heated the electrons to temperatures as high as 100eV. Re-examination of the original diffusion model showed that it was capable of producing equal to or greater than the expected mobility. Results described here use the original anomalous diffusion model from [1] with a Hall parameter of 400. A more detailed examination of the diffusion model is presented in chapter 4.

2.3 P5 Geometry

The P5 is an SPT-type Hall thruster developed at the University of Michigan, Ann Arbor [7]. Of particular interest for this study are the wall materials and thruster dimensions. The discharge chamber walls are made of a 50% Boron Nitride (BN) and 50% Silicon Dioxide (SiO2) ceramic. The inner pole piece guard disk is made of pure Boron Nitride, although no distinction between the chamber and the guard disk materials is made in this simulation. The anode and the front outer pole, the only other solid pieces in the simulation, are composed of stainless steel and iron respectively. Figure 2-1 shows these features under the 88 by 96 node grid. As shown, the simulation region extends 4 cm downstream from the chamber exit and down to the thruster centerline. The discharge chamber is 25mm wide and 38mm long.

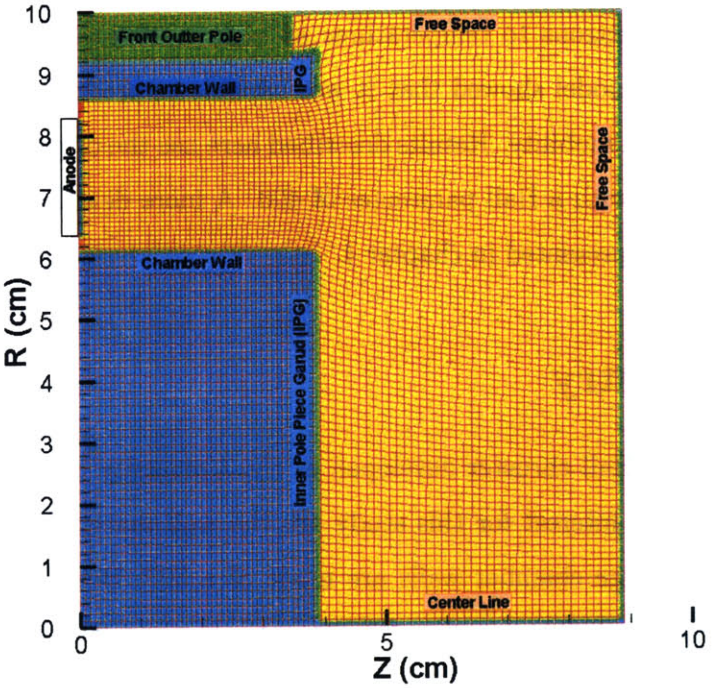
Front Outter Pole
Chamber Wall
IPG
Free Space
Anode
Free Space
Chamber Wall
Inner Pole Piece Garud (IPG)
Center Line
10
9
8
7
6
5
4
3
2
1
0
R (cm)
0
5
10
Z (cm)

Figure 2-1: P5 Grid

Chapter 3

P5 Results

3.1 Conditions for Current Runs

The current grid has $88x96$ cells. In the center of the chamber, the average cell length is $0.8mm$, and the cell volume is $0.296cm^3$. A mass factor of 1000 and an artificial permittivity of 1600, result in a maximum artificial Debye length of approximately 1mm, which is still much smaller than, for instance, the channel width of the P5 (25mm). The maximum electron plasma frequency and Larmor frequency are both on the order of $10^8 Hz$, resulting in a time step of approximately $10^{-10}s$ per iteration. With this time step and mass factor, neutrals take approximately 140,000 iterations to clear the chamber. The anomalous Hall parameter is set to 400. The radial magnetic field strength and field lines are shown in figure 3-1. (This field was given to MIT by the University of Michigan in Anne Arbor.) The peak field strength is adjusted proportional to $\sqrt(V)$ in order to keep the Larmor radius constant; a procedure that should produce optimal efficiency in SPT-type Hall thrusters [2].

3.2 Simulation Results

We tested the simulation of the P5 at 3kW and 5kW. Experimental data from James Haas [3] were used to check results. Haas took extensive measurements at 3kW and also gave performance data for 5kW operation. All settings except the anode voltage,

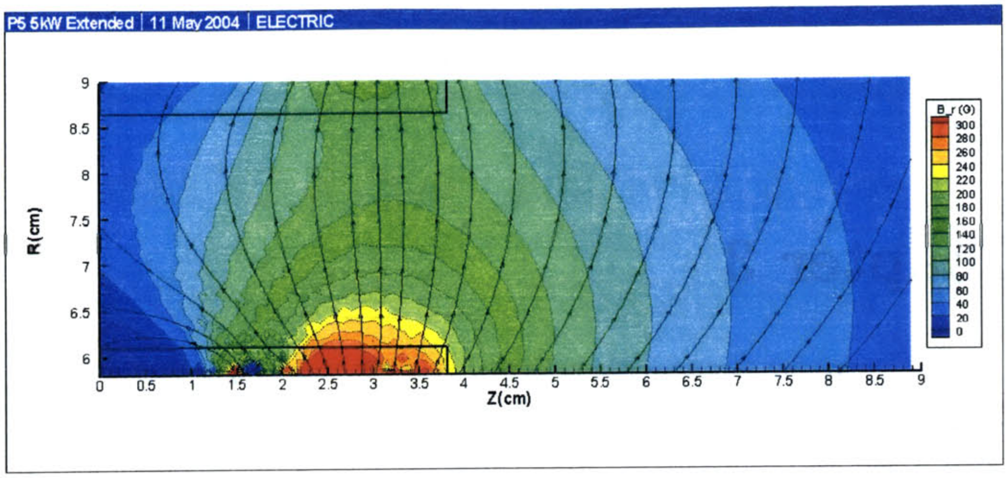

Figure 3-1: Radial Magnetic Field used at MIT

maximum magnetic field, and neutral flow rate were the same between the runs. A comparison of the simulated and experimental performance data is listed in table 3.1.

Table 3.1: Summary of Code and Experimental Thruster Performance

	3kW PIC	3kW Haas	5kW PIC	5kW Haas
Maximum B (G)	290G	250	360	360
Anode Voltage (V)	300	300	500	500
Anode Current (A)	7.5	10	7.4	10
Mass Flow Rate (mg/s)	11.41	10.74	10.83	10.83
Thrust (mN)	180	180	226	240
ISP (s)	1600	1650	2210	2300
Efficiency	0.63	0.48	0.64	0.57
Oscillation Freq (kHz)	6.5	N/A	11.7	11

The code correctly predicts thrust and specific impulse, but under predicts the anode current by 25% at both power settings. The main oscillation frequency observed in the plasma, after being corrected for the artificial permittivity, matches the anode current oscillation frequency observed by Haas.

A more detailed look into the thruster operation shows that most phenomena are concentrated closer to the anode and over a larger region than expected from the experimental results. Time-averaged plasma potential simulations, figure 3-3, show a gradual drop towards the anode, while the probe data, figure 3-2 show a high potential filling most of the chamber and dropping suddenly near the chamber exit. At 3kW the simulated and measured potentials both exhibit a bowing out near the center of the chamber exit that is much weaker at other voltages. Along the bottom wall, at both simulation conditions, there is an area of positive charge and an inverted sheath. This may be due to a lack of particles in the bottom half of the chamber.

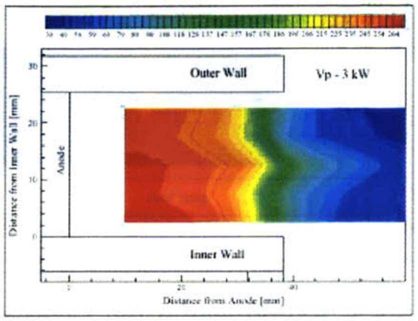

Figure 3-2: Experimental Plasma Potential 3kw [3]

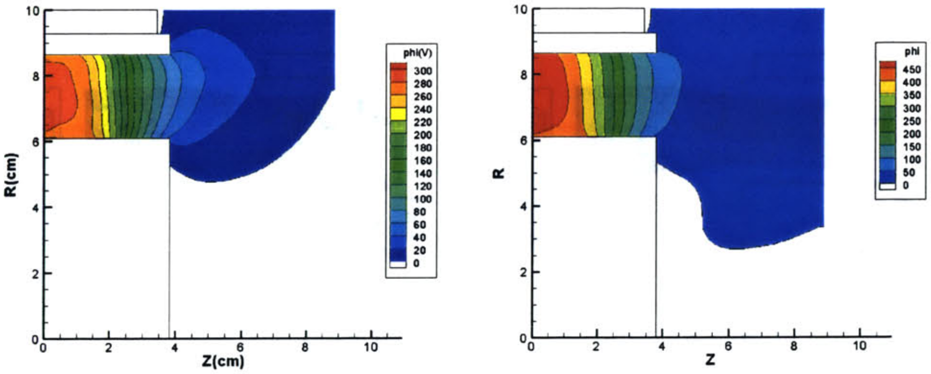

Figure 3-3: Average Plasma Potential 3kw (left) and 5kw (right)

The time-averaged ion density peak, figure 3-5, is of the right magnitude, but is severely shifted toward the anode compared to the probe data, figure 3-4. The simulated ion density profile is also much wider than measured experimentally. Haas shows the ion density peaking at the channel exit and almost immediately dropping off upstream. The simulation results show medium to high densities filling the chamber in a fish-like shape. Figure 3-6 shows that the peak ionization is right on top of the anode. While this is consistent with the density peak near the anode, the peak ionization region should be near the end of the chamber in the area of maximum magnetic field. The peak densities of Xe++ ions is further down stream, figure 3-7, but the number of Xe++ ions is insignificant compared to the number of Xe+ ions.

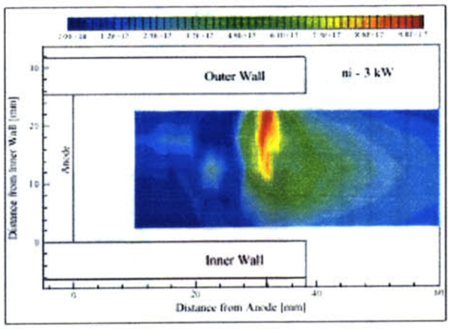

Figure 3-4: Experimental Ion Density 3kw [3]

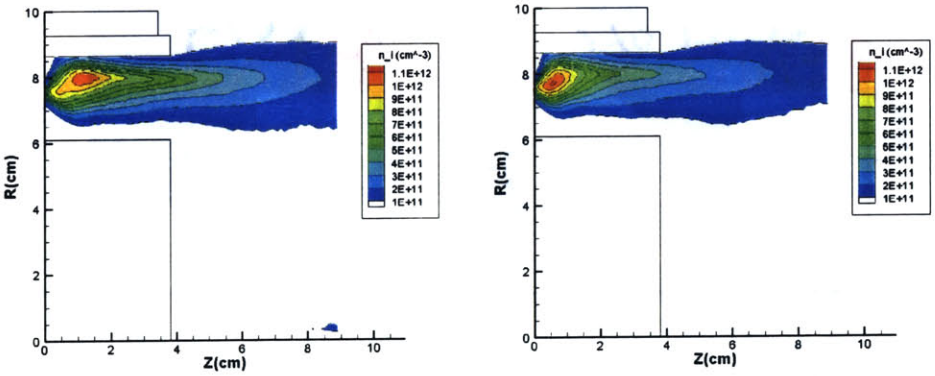

Figure 3-5: Average Ion Density 3kw (left) and 5kw (right)

The average electron temperatures in the chamber, shown in figure 3-9, are lower than those observed experimentally, figure 3-8 by about 10eV, but have approximately the correct shape and concentration. Both the measured and simulated temperatures are concentrated between 20 and 35mm down the chamber, although the simulated results are slightly shifted towards the anode.

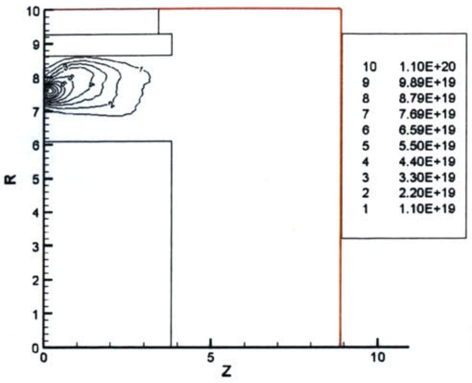

Figure 3-6: Average Neutral to Single Ionization Rate 3kW

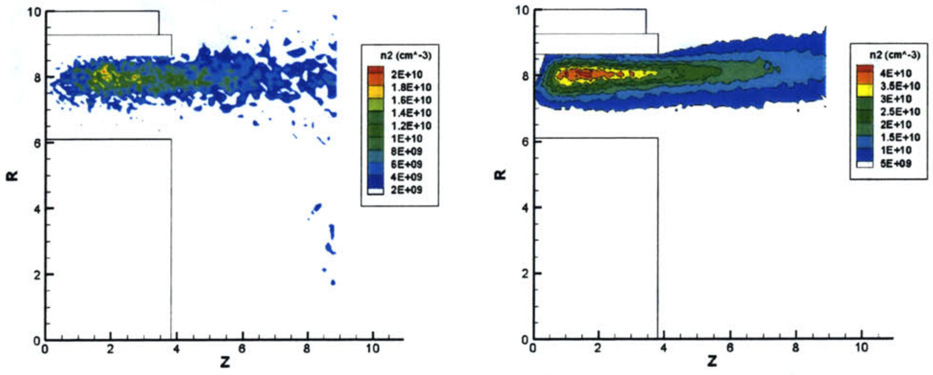

Figure 3-7: Average Xe++ Distribution 3kw (left) and 5kw (right)

3.3 Effect of Increased Voltage

The results at 500V very closely resemble those at 300V. The plasma potential falls at relatively the same rate in the channel, figure 3-3. The ion density peak is concentrated closer to the anode, but is of a similar magnitude, figure 3-5. The peak double ion density is doubled but in a similar location, figure 3-7, and still does not approach the same order of magnitude as the single ion density. The electron temperature is found closer to the outer dielectric wall, and as expected, has increased with the anode voltage, figure 3-9.

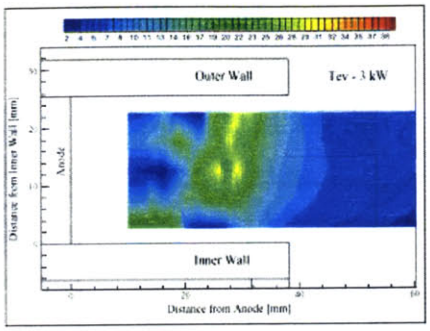

Figure 3-8: Experimental Electron Temperature 3kw [3]

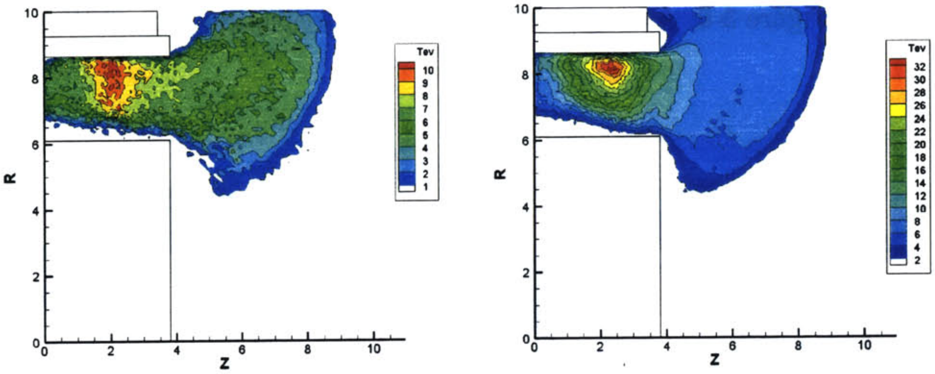

Figure 3-9: Average Electron Temperature 3kw (left) and 5kw (right)

3.4 Evolution of density and temperature

Following the operation of the thruster over time shows deep oscillations at a frequency much lower than plasma frequency. The magnitude of these oscillations shrinks as the anomalous diffusion is reduced and becomes more severe as the anomalous diffusion is increased. Oscillations also become less severe with higher voltage. Figures 3-10, 3-11, 3-12, 3-13 show ion density profiles at the half-way-to-maximum, maximum, half-way-to-minimum, and minimum current peaks. When rising, the ions form the fish-shape seen in the time averages. As the current falls, the ions become less concentrated, ending in isolated patches of ions at time of minimum current.

The electron temperature, figures 3-14, 3-15, 3-16, 3-17, is out of phase from the ion density by a quarter cycle. When the current and ion density is rising, the electron temperature is at a minimum. When the current is falling, the electron temperature is at a maximum. The temperature peak approximately corresponds to the axial location of peak magnetic field magnitude. The temperature in the plume decreases as the temperature in the chamber increases.

3.5 Discussion

While we have successfully simulated the P5 at 3kw and 5kw operation, several discrepancies exist between our simulation results and experimental results. The major issues with the full simulation results are the high Hall parameter, an ionization region located very near the anode, and the collapse of the bottom sheath. Most of our subsequent work focuses on rooting out the cause of these problems. In [8], we speculated that either the axial electron mobility was still elevated, despite the reduced anomalous diffusion, or that there were unaccounted for mechanisms artificially enhancing the ionization rates, or that the probe data underestimated the electron density near the anode. The next two chapters will reexamine the particle transport mechanisms and simulation inputs for significant improvements to our results.

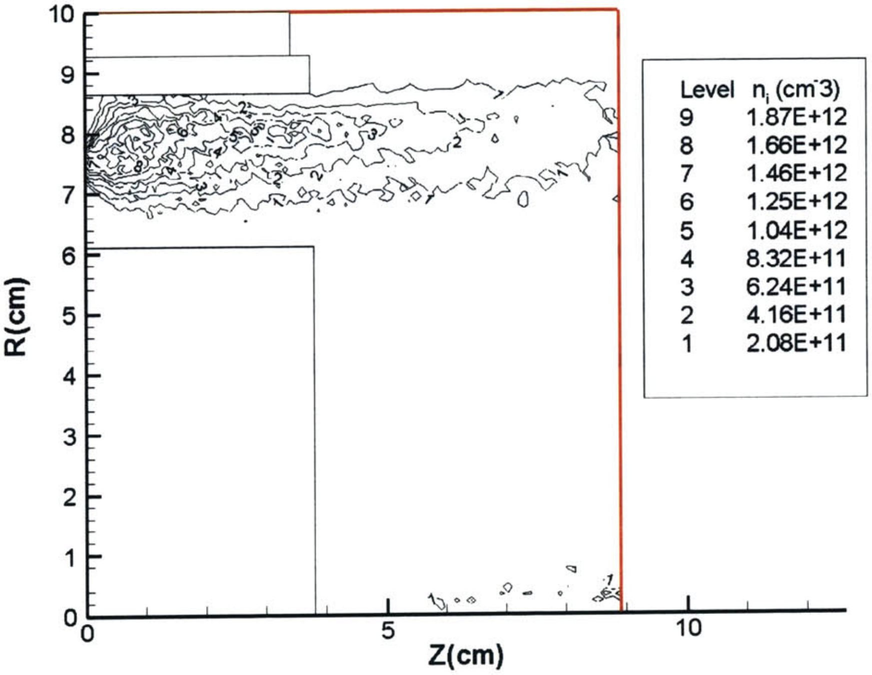

Figure 3-10: Rising Ion Density 5kw

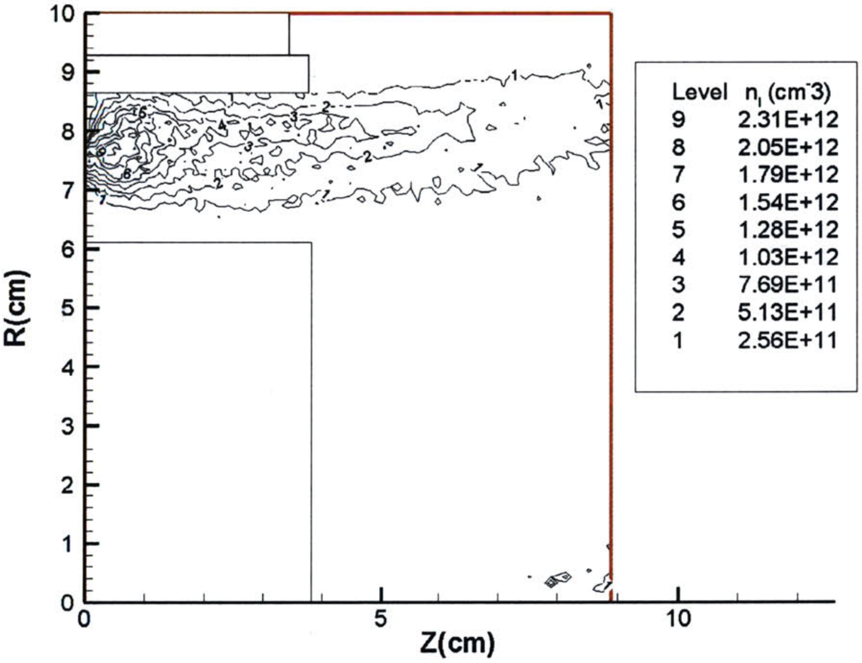

Figure 3-11: Maximum Ion Density 5kw

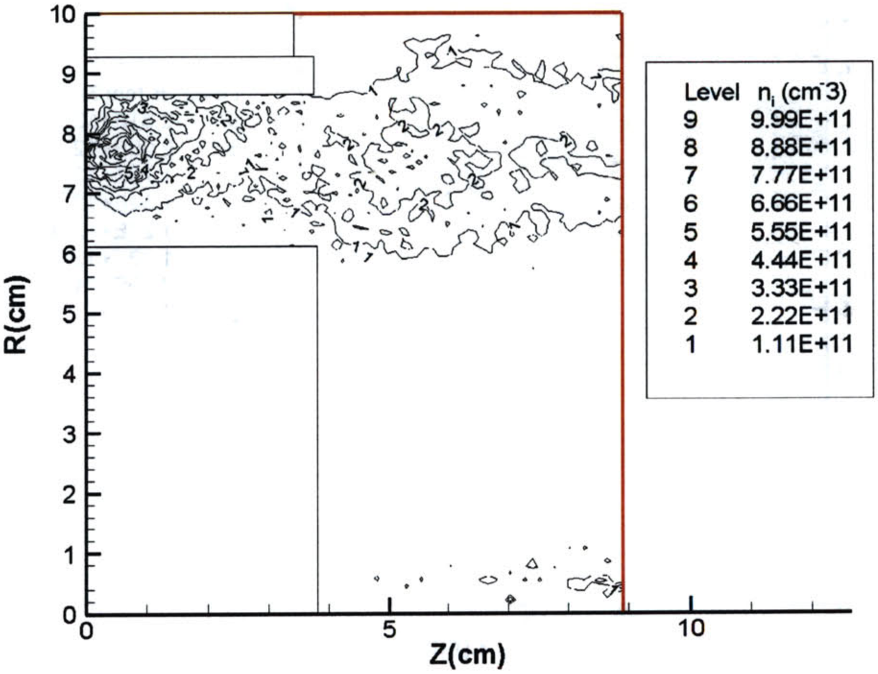

Figure 3-12: Falling Ion Density 5kw

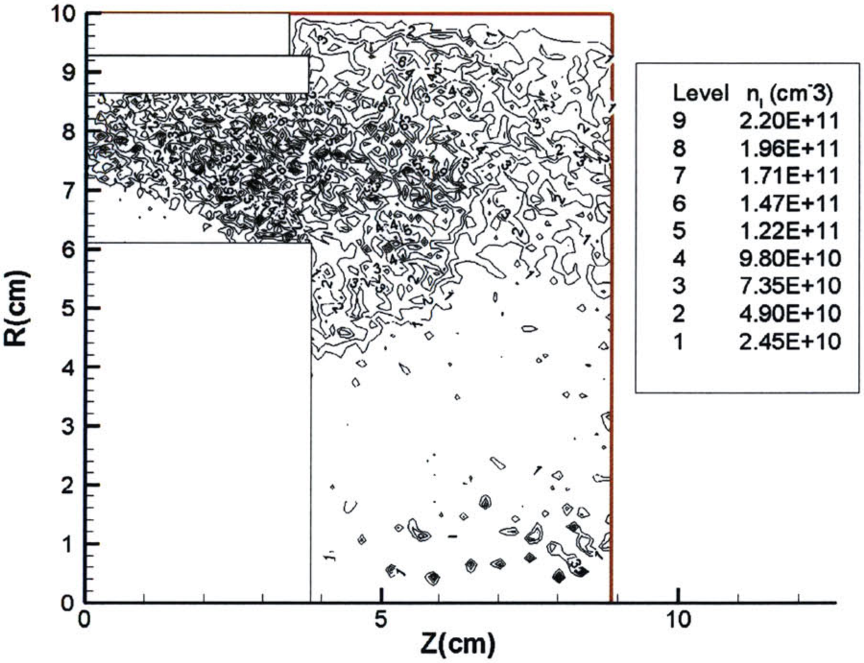

Figure 3-13: Minimum Ion Density 5kw

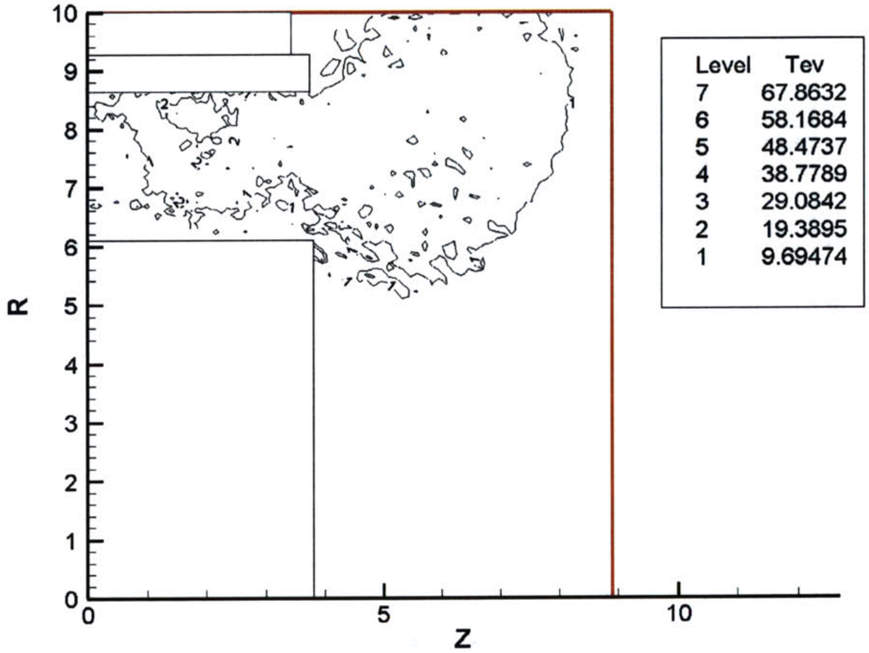

Figure 3-14: Rising Electron Temperature 5kw

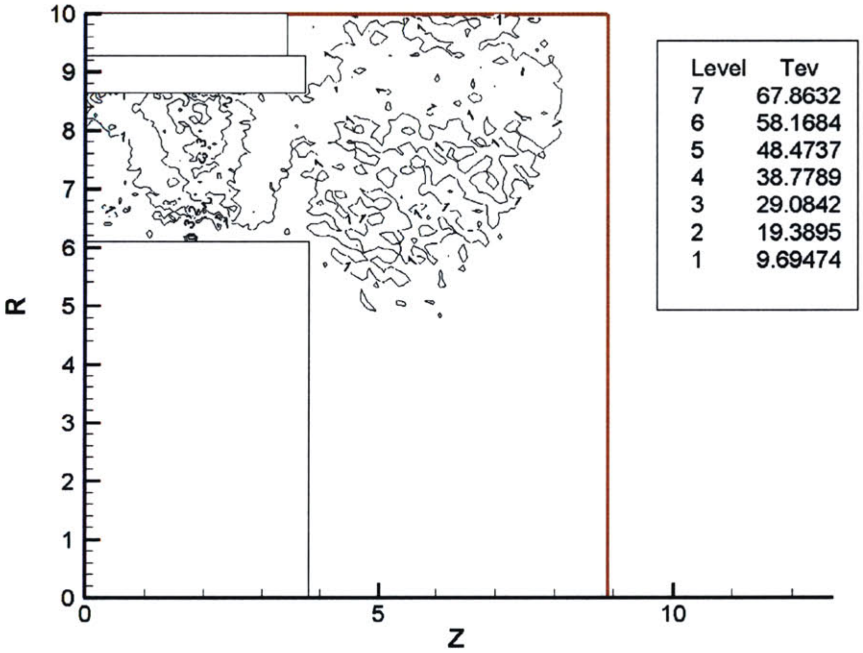

Figure 3-15: Maximum Electron Temperature 5kw

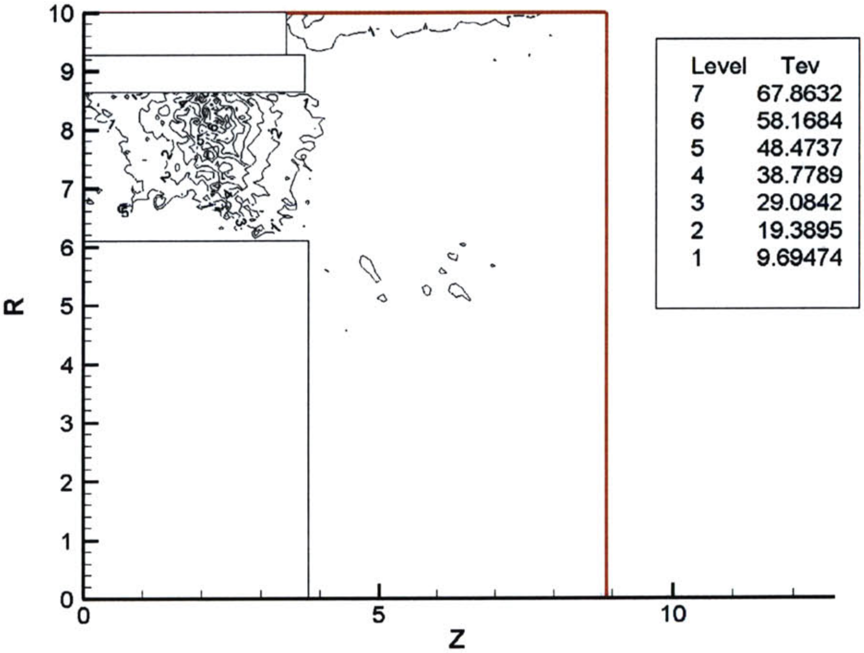

Figure 3-16: Falling Electron Temperature 5kw

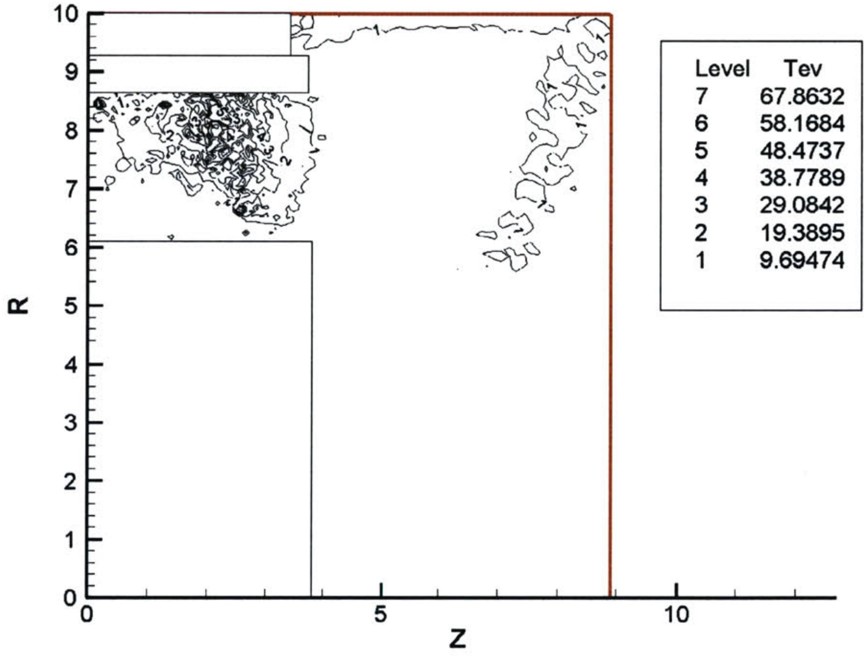

Figure 3-17: Minimum Electron Temperature 5kw

Chapter 4

Electron Transport

4.1 Anomalous Diffusion

Anomalous diffusion is modelled via a modification of Bohm's diffusion formula

$$D_{ano} = \frac{kT_e}{\beta' eB} \tag{4.1}$$

where the anomalous Hall parameter β' is chosen parametrically. The current procedure is to execute additional collisions over and above the number indicated by the existing densities and cross sections. The frequency ν_{ano} of these extra collisions follows from equating 4.1 to the classical expression

$$D_{class} = \frac{kT_e}{m_e} \frac{1}{\omega_c} \frac{\beta}{1+\beta^2} \tag{4.2}$$

where $\beta = \frac{\omega_c}{(\nu_{ano}+\nu_{classic})} = \frac{\omega_c}{\nu_{tot}}$.

For low collisionallity $\nu_{tot} << \omega_c$ the solution is

$$\beta = \frac{\beta' + \sqrt{\beta'^2 - 4}}{2} \simeq \beta' \tag{4.3}$$

The anomalous collision frequency is extracted by calculating the classical collision frequency

$$\nu_{classic} = \sum Q n_n v_e = \nu_{Xe+} + \nu_{excite} + \nu_{scatter} \tag{4.4}$$

and subtracting it from the total collision frequency such that

$$\nu_{ano} = \nu_{tot} - \nu_{classic} = \frac{\omega_c}{\beta'} - \sum Q n_n v_e \tag{4.5}$$

Note that due to the square root term in equation 4.3, β' must be greater or equal to 2. A stricter limit also exists because the code, as currently implemented, can only calcuate one collision event per electron per iteration, meaning $\nu_{tot}dt \leq 1$. The time step is on the order of $\frac{1}{3}\frac{2\pi}{\omega_c}$, which after some manipulation leads to the condition $\beta' \geq 2.09$. If the stricter condition described in [2], $\nu_{tot}dt \leq 10$, is used to reduce the probability of two or more anomalous collisions occuring in one timestep, the restriction on the Hall parameter becomes $\beta' \geq 20.9$.

As mentioned in chapter 2, all collision frequencies must be increased by $\sqrt{f}$ in order to be correct relative to the increased ion flux. This is acomplished by replacing β' with $\frac{\beta'}{\sqrt{f}}$ and multiplying the classical collision cross sections by $\sqrt{f}$. Taking the mass factor into acount effectively increases the lower bound on β'. Now $\frac{\beta'}{\sqrt{f}}$ must be greater than 2.9. The minimum Hall parameter with a mass factor of 1000 is 66. If the stricter probability condition is used, the Hall parameter must exceed 660!

The originally recommended β' parameter is 16, but other researchers [1], [9] have found that best agreement with performance data in Hall thrusters requires a larger value, of the order of 64. This value is also supported by direct simulation results presented by Batishchev [10]. In our numerical work on the P5 thruster, we have found that even these larger values of β' (which imply a reduced level of anomalous mobility) are insufficient, and that best performance and oscillation results require $\beta' \approx 200 - 400$. Figure 4-1 shows computed current versus time for a series of test runs using different β' values. It can be seen that lower values of β' normally lead to either divergence or extinction of the discharge and to clearly inaccurate average current in any case.

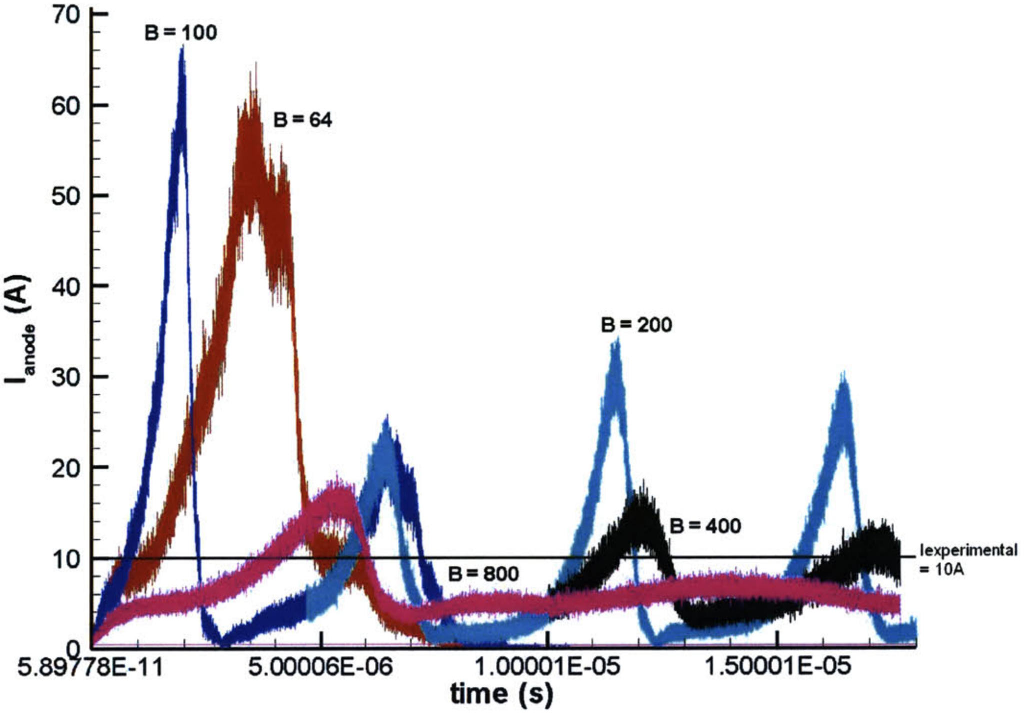

Figure 4-1: Anode Current versus Time for Various Hall Parameters.

4.2 Isolated Mobility Tests

In order to investigate this effect, a series of test cases were devised in which the plasma geometry of the P5 was retained, but most of the dynamics were suppressed. Heavy particles were frozen in place, the electric field was fixed as a purely axial and uniform field, and the magnetic field was made uniform and radial. The Poisson solver was turned off, and a self-consistent sheath was not calculated. A large number of electrons were tracked in these fields, and their mean axial velocities recorded after many collisions and many gyrations. The results of these tests were at first surprising, in that the implied electron cross-field mobility was typically several times greater than could be calculated from equation 4.2 plus Einstein's relationship $\frac{\mu}{D} = \frac{1}{kT}$. Upon closer inspection, it was found that a significant, sometimes dominant, contribution to the axial displacement was due to secondary electron emission from the ceramic walls.

Since the secondary electron is emitted in a random direction, there is an average displacement against the field associated with these events. Figure 4-2 shows a portion of a trajectory in which this effect was captured. When the secondary emission was also artificially suppressed, the computed mobility agreed with the calculation based on collision frequency, figure 4-3.

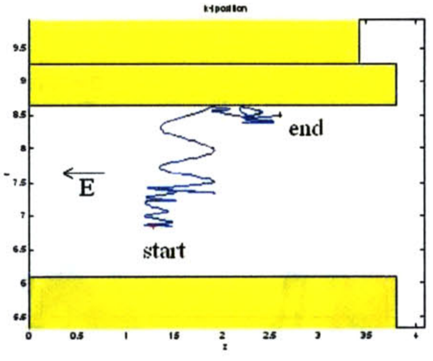

Figure 4-2: Primary to Secondary Electron Trajectory, inverted electric field

This 'wall conductivity' is, of course, not a new phenomenon, and its existence, in association with secondary emission or with diffuse scattering from walls has been postulated in the Russian literature for many years. However, based on estimates derived from 1D modelling work [11] we had not expected it to be significant, except perhaps locally in the highest electron temperature region.

4.3 Wall Effects in the Full Simulation

In an attempt to verify the effect of secondary electron emission (SEE) on the full simulation, runs were preformed with SEE turned off. Based on the isolated tests, when SEE is eliminated, all other things being constant, anomalous transport should decrease. We therefore ran with lower anomalous Hall parameters, 200 and 64, to compensate.

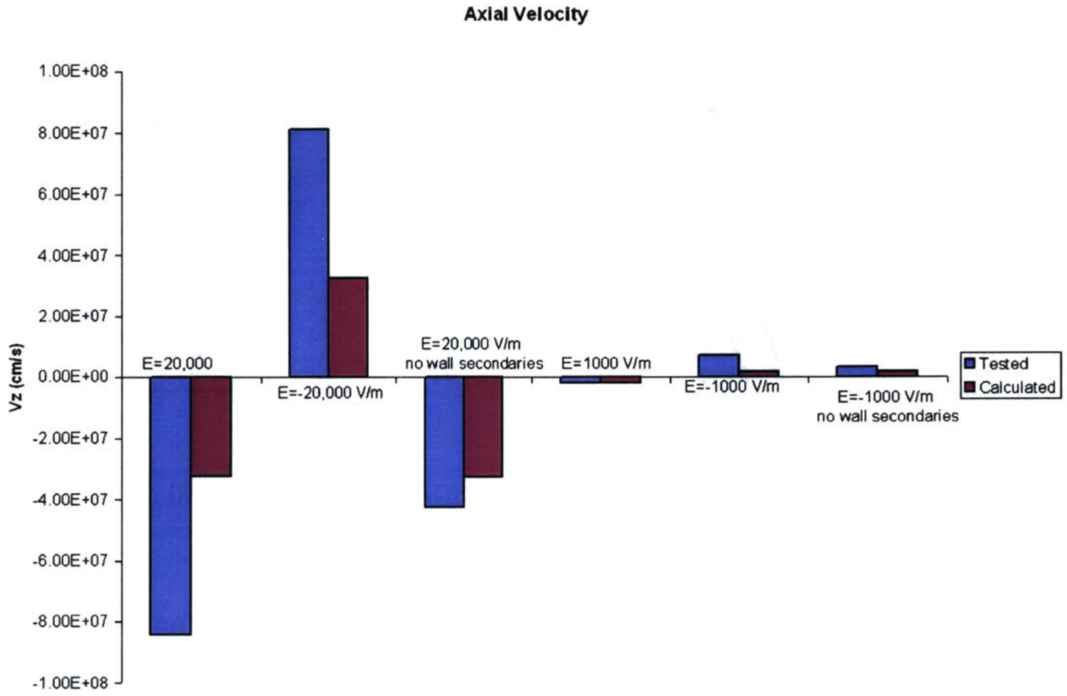

Figure 4-3: Summary of Electron Cross-Field Velocity. Tested indicates average simulated axial electron velocity. Calculated velocities are from $\mu_{tot} = \frac{e\sum\nu}{m_e\omega_c^2}$, using simulated collision frequencies and field strengths.

4.3.1 Results

There are few differences between the normal simulation and the simulation without SEE. Comparing the two cases at a $\beta' = 200$, we find the peak electron temperature is now in the middle of the channel instead of closer to the upper wall, see figure 4-4, although the temperatures are the of the same magnitude. The particles fill more of the chamber with no SEE, figure 4-5, but the bottom sheath still collapses, although at a point further up stream, see figures 4-6 and 4-7.

There is also no indication that the lack of SEE made a significant contribution to the electron mobility. Due to the complex field geometry, it is difficult to get a direct measurement of electron mobility, however the anode current is an indicator of how many electrons travel across the magnetic field lines. The anode current, shown in 4-8 is nearly identical between runs with the same Bohm coefficient regardless

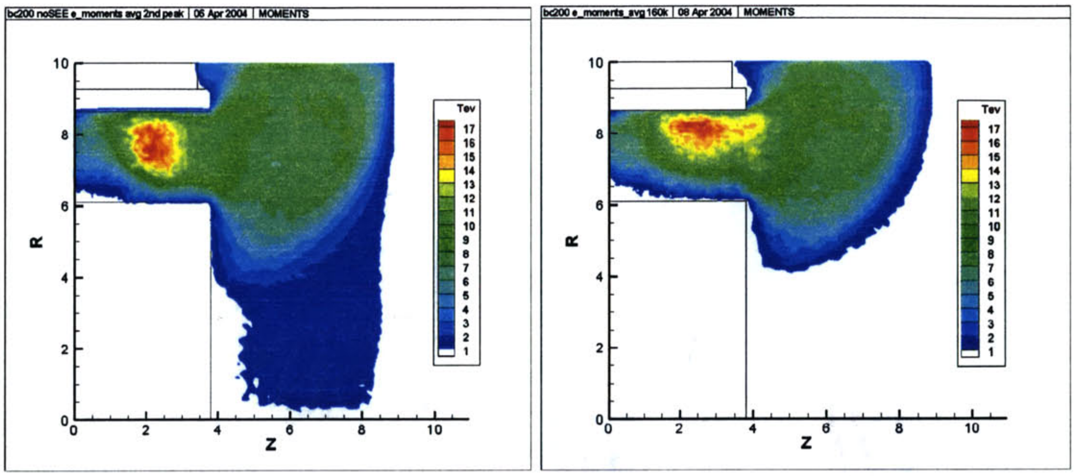

Figure 4-4: Average Electron Temperature with No SEE (left) full $\beta' = 200$ run (right)

of secondary electron emission, however, the anode current may not be the best indicator of cross-field mobility in our case because the major ionization region is so far upstream. If the majority of electrons are generated in the ionization region, then the majority of electrons do not have very far to travel to reach the anode.

4.3.2 Results with Radial B Only

To directly obtain an indicator of electron transport, we calculated the electron mobility $\mu = \frac{v_\perp}{E_\perp}$ in runs using the purely radial magnetic field with and without secondary electron emission. As described in chapter 5, using a purely radial magnetic field allowed the particles to fill the entire chamber and a sheath to form along both walls, although the peak ionization location was unchanged. It also allowed us to easily find the perpendicular velocity and electric field components in each cell.

The simulated and theoretical electron mobilities are calculated in each grid cell using data averaged over 80,000 iterations. The simulated mobility is defined as $\mu_{sim} = \frac{v_z}{-E_z}$. The theoretical mobility is made up of two parts, Bohm mobility and classical mobility. The Bohm mobility is defined as $\mu_{Bohm} = \frac{\sqrt{f}}{400 B_r}$. The $\sqrt{f}$ factor is a consequency of increasing all collision frequencies to keep up with increased heavy particle fluxes. The mass factor f is equal to 1000 in all of the runs presented here.

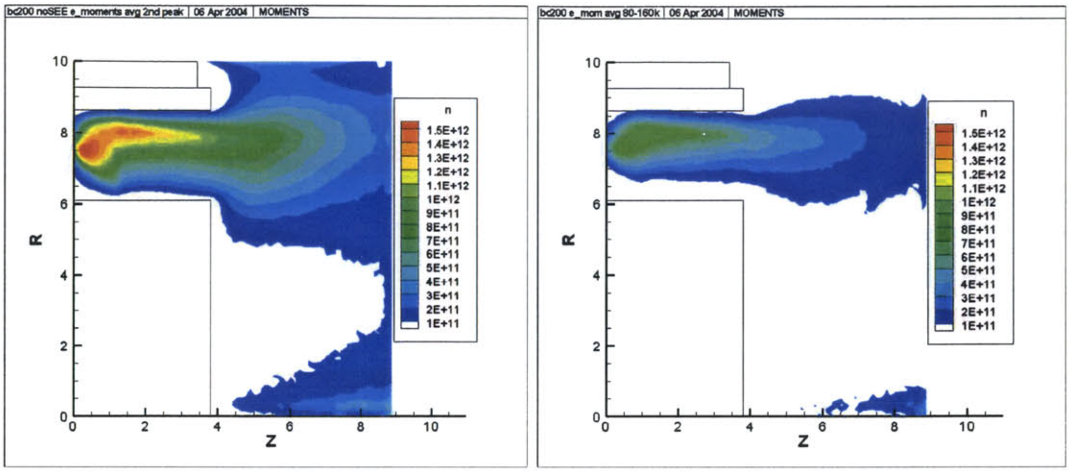

Figure 4-5: Average Electron Density with No SEE (left) full $\beta' = 200$ run (right)

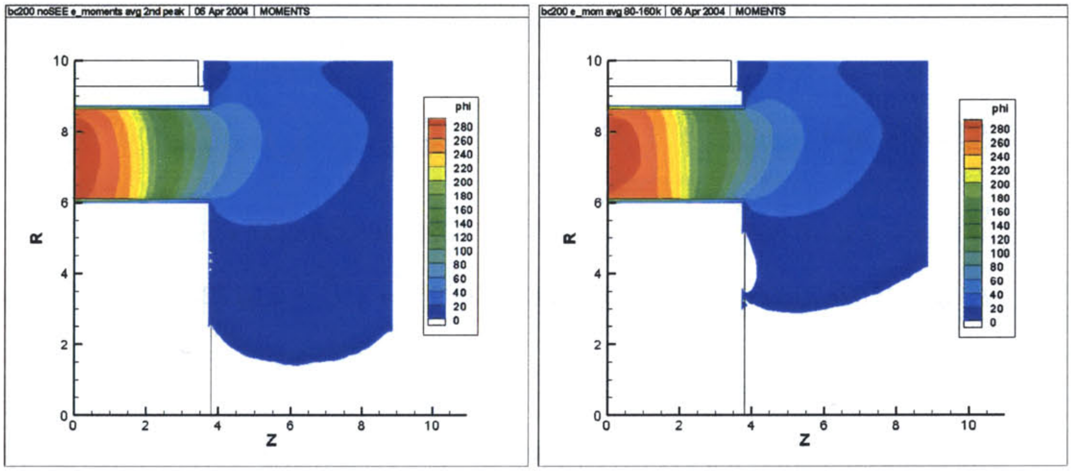

Figure 4-6: Average Plasma Potential with No SEE (left) full $\beta' = 200$ run (right)

The mobility perpendicular to the magnetic field due to classical collisions is defined as $\mu_{classical} = \frac{e\nu_{tot}}{m_e\omega_c^2}$. Where $\nu_{tot} = \nu_{Xe+} + \nu_{excite} + \nu_{scatter}$ and ω_c is the electron cyclotron frequency $\omega_c = \frac{qB}{mc}$. Because the code does not currently report the total collision frequency, it must be estimated from $\nu_{tot} = Q_t\sqrt{f}n_n < v_e >$. The total collision cross section, Q_t, is approximated by a polynomial fit to experimental data, see [1]. In the energy ranges of interest here, those polynomials, which are also used in the code, are

$$Qt = 1.0e - 13(0.07588072747894 * E^2 - 0.34475940259139 * E * \sqrt{E}$$

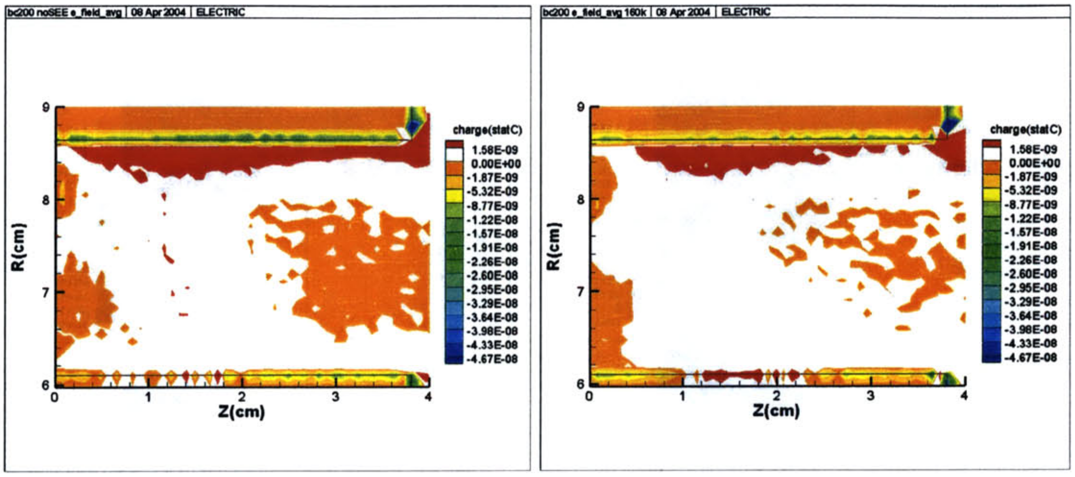

Figure 4-7: Average Charge with No SEE (left) full $\beta' = 200$ run (right)

$$+ 0.58473840309059 * E - 0.42726069455393 * \sqrt{E} + 0.11430271021684)cm^2$$

for $E \leq 2.8eV$ and

$$Qt = 1.0e - 13(-0.00199145459640 * E^2 + 0.02974653588357 * E * \sqrt{E}$$
$$- 0.16550787909579 * E + 0.40171310068942 * \sqrt{E} - 0.31727871240879)cm^2$$

for $2.8eV < E \leq 24.7eV$.

Averaging the simulated, classical, and Bohm mobilities over the regions defined in figure 4-9 (chamber indicates the entire discharge chamber) produces table 4.1. The bottom region is probably too sparsely populated to give an accurate indication of the electron velocity there.

Averaging throughout the chamber, the electron transport is governed by the classical collisions because of the large collisionality near the anode. This is the region of highest particle densities (of all species) and highest ionization rates. In the downstream half of the chamber, nearly all of the mobility is accounted for by the μ_{Bohm}. Including the walls in the averaging region (half chamber w/walls) shows a slight increase in simulated mobility, around 20%, without a corresponding increase in either of the theoretical mobilities.

When secondary electron emission is turned off, table 4.2, we see the same pattern

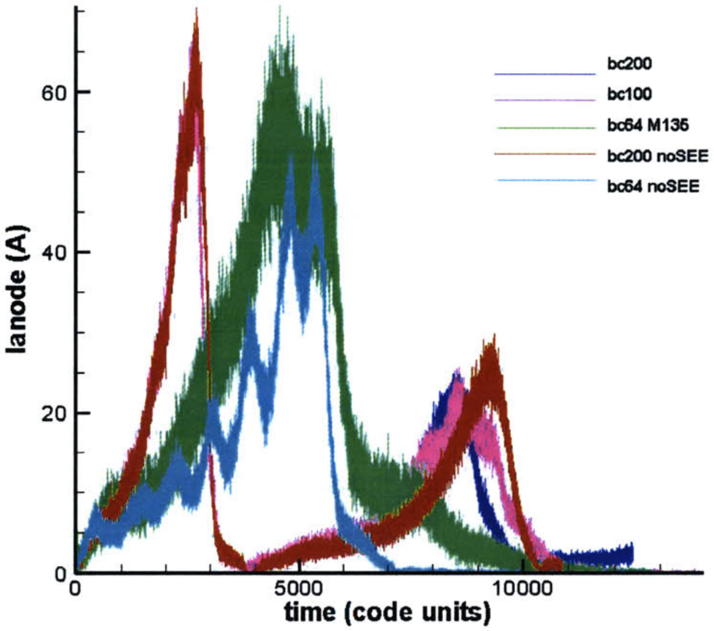

Figure 4-8: Comparing anode current with and without SEE

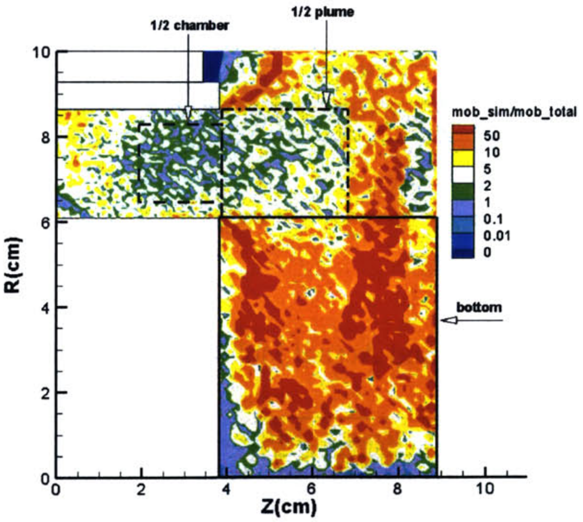

Figure 4-9: Ratio of μ_{actual} to μ_{total}

of behavior. There is a significant increase in the clasical and simulated mobility in the chamber with no SEE (as compared to table 4.1), despite similar electron temperatures, electron velocities, and neutral densities between runs. In areas with low classical collisionality, i.e. the half chamber and half chamber with walls regions, there is a 25% decrease in the simulated mobility when SEE is removed, but not the half decrease observed earlier in the isolated tests. With no SEE there is still a 20% increase in simulated mobility when including the walls in the half chamber averaging region. Note that turning SEE off brings the simulated mobility down to theoretical levels in the bottom and plume regions. The plume region is defined as the top right corner of the simulation region, or everything that is not the 'bottom' and the 'chamber'. The half plume regions is as shown in figure 4-9. This strong effect of SEE is surprising because there are very few electron impacts at all with the vertical walls, much less SEE, and may indicate a bug in the code.

Table 4.1: Theoretical Bohm and Actual Mobility Averaged over Grid Region ($\frac{m/s}{V/m}$)

region	μ_{Bohm}	$\mu_{classical}$	$\mu_{Bohm} + \mu_{classical}$	μ_{sim}
bottom	63.8415	0.4791	64.3206	552.26056
chamber	6.8208	44.4958	51.3166	45.1380
half chamber	5.5012	0.0583	5.5595	6.3367
half chamber w/walls	5.3818	0.0631	5.4450	7.6274
plume	14.4781	0.0154	14.4935	223.0618
half plume	8.8382	0.0100	8.8482	9.8260

Table 4.2: Theoretical Bohm and Actual Mobility Averaged over Grid Region no SEE ($\frac{m/s}{V/m}$)

region	μ_{Bohm}	$\mu_{classical}$	$\mu_{Bohm} + \mu_{classical}$	μ_{sim}
bottom	63.8415	1.1689	65.0104	30.1337
chamber	6.8208	89.6846	96.5054	63.3367
half chamber	5.5012	0.0261	5.5273	4.6640
half chamber w/walls	5.3818	0.0443	5.4261	5.7332
plume	14.4781	0.0040	14.4820	5.1389
half plume	8.8382	0.0043	8.8425	6.2910

4.4 Discussion

The effects of anomalous diffusion and secondary electron emission were explored for the full simulation and simplified test cases. While SEE was responsible for half of the observed electron mobility in simplified tests, secondary electron emission was not a dominant effect in the full simulation, although its influence could be seen in areas with low classical collisionality. A possible reasons for the discrepancy in this regard between the isolated tests and the full runs is that in the full simulation, the level of secondary electron emissions has a strong influence on the level of classical collisionality. With ionization suppressed in the earlier isolated tests, elimination of SEE halved the average axial electron velocity. The doubling of classical collisions would increase the total mobility, accounting for the transport lost due to no SEE, at least in regions where high neutral densities could support the increased ionization and scattering rates. (See appendix A.)

Classical collisions were shown to be the overwhelming mechanism of electron transport in the near-anode region, while anomalous diffusion was almost solely responsible for mobility in all other parts of the simulation. We also observed the limited ability of collisions to produce mobility in areas where either anomalous or classical collisions resulted in total mobilities on the order of 10s of $(\frac{m/s}{V/m})$. We have so far, however, failed to identify the reason for the apparent need of an unexpectedly high β' factor.

Chapter 5

Examining the Magnetic Field

5.1 Magnetic Mirroring

The main cause for the collapse of the bottom sheath seems to be a lack of particles impacting on the bottom wall. The first suspect is a magnetic mirroring effect. The magnetic field lines do curve more severely near the bottom wall than near the top wall. The fraction of isotropic electrons that can reach the wall is $\frac{1-\cos\theta}{2}$, where θ is found from the mirroring condition $\sin\theta = \sqrt{B_{min}/B_{max}}$. Near the exit of the chamber $B_{min} = 131G$ and $B_{max} = 268G$, giving a θ of 44° and an acceptance fraction of only 0.14. In the center of the chamber, where the magnetic field curvature is strongest $B_{min} = 97.3G$ and $B_{max} = 305G$, giving an acceptance fraction of 0.09. The vast majority of an isotropic electron population, 90%, is being repelled from the bottom wall by magnetic mirroring. This explains why there is a lack of particles in the bottom half of the discharge chamber.

5.2 Simplified Magnetic Field

The simplest way to isolate the influence of the magnetic field curvature, i.e. mirroring, while retaining all other dynamics is to fix the magnetic field as purely radial. We zeroed the axial component of the old magnetic field and ran a full simulation. With this method the perpendicular components of velocity, temperature, etc are simply the axial and theta components in each cell, and the electric and magnetic fields are everywhere nearly perpendicular to each other. Contours of the radial component and the modified field lines are shown in figure 5-1. While this field is physically inconsistent, since it will not satisfy $\Delta \cdot \bar{B} = 0$ and $\Delta \times \bar{B} = 0$, it is acceptable for the purpose of eliminating the bottling effect. A Hall parameter 400 is used with an anode voltage of 300V, a mass factor of 1000, and a gamma factor of 40.

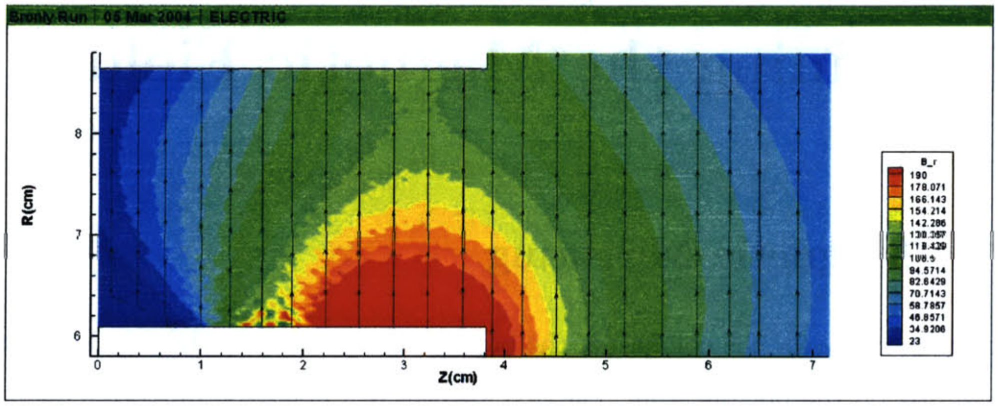

Figure 5-1: Simplified Radial Magnetic Field

The results time-averaged over the start-up oscillation exhibit nice, symmetric contours where before the bottom section of the chamber lacked particles and the bottom wall was positively charged, see figure 5-2. The ions and electrons completely fill the chamber with a symmetric fishtail shape, the only difference between them being a nearly-electron-free region three cells wide along both walls. Three cells cover approximately three modified Debye lengths, and using three cells as the sheath width yields a sheath strength of around 10V, figure 5-3. Electron temperatures near the wall range from 3eV along the bottom wall near the chamber exit, and 20eV towards the center of the top wall, figure 5-4.

This run confirms the ability of the simulation to calculate a sheath on both walls. The lack of a sheath in previous runs is due to a lack of particles hitting the wall. The lack of particles is in turn due to the shape of the magnetic field and magnetic mirroring. The peak ionization region, and therefore the peak charged particle density, is unaffected and is still near the anode instead of the chamber exit.

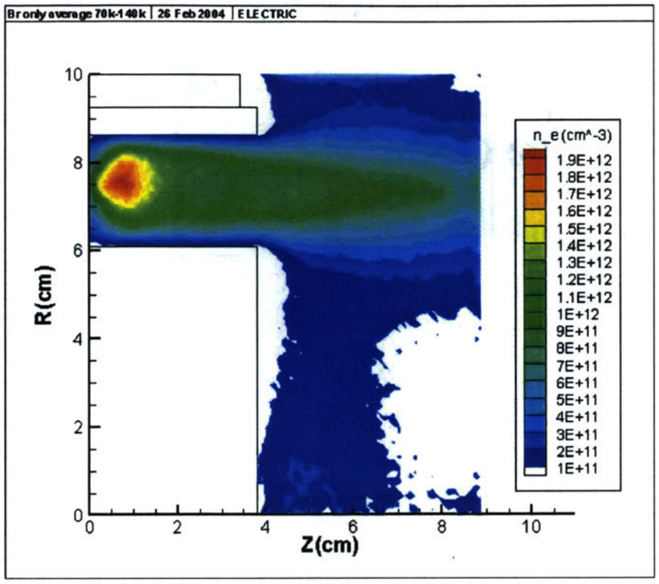

Figure 5-2: Br only average electron density

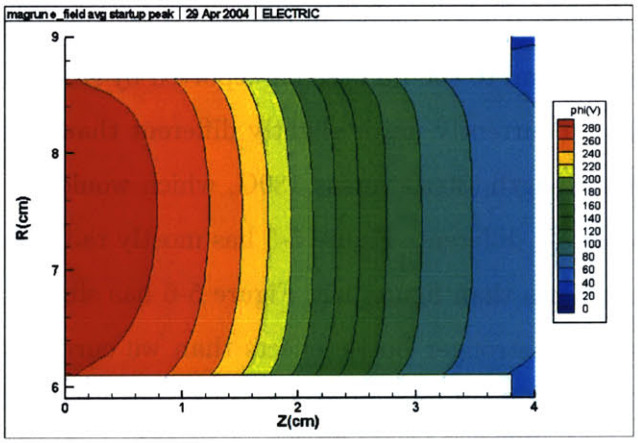

Figure 5-3: Br only average plasma potential in the channel

5.3 New Magnetic Field

Upon closer inspection, the magnetic field used thus far in our simulation, figure 3-1, is not the field reported in [3]. We have recently obtained two new magnetic field files courtesy of Justin Koo at the University of Michigan Ann Arbor. One of the new fields is used by Koo in a hybrid-PIC simulation [12] and appears to be identical to the field reported in [3], figure 5-5. The other, figure 5-6, which covers our entire simulation region, appearers to correspond to the P5's magnetic field without magnetic screens,

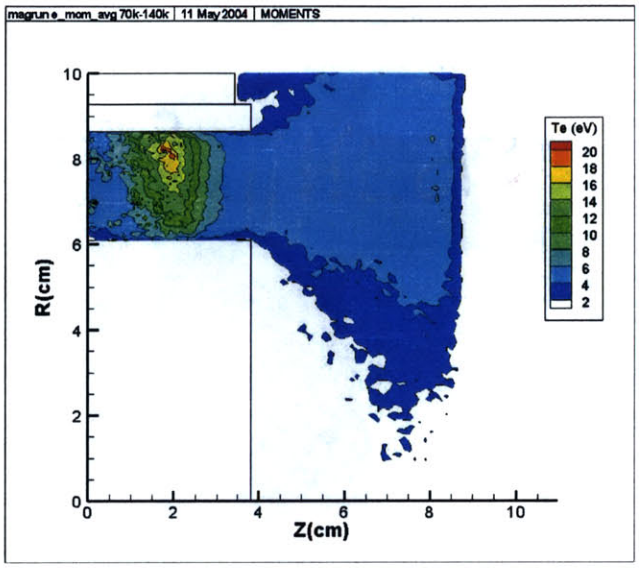

Figure 5-4: Br only average electron temperature

([13] figure 5.12d case 4). (Note, based on the field lines, the magnetic field we have been using may correspond to the P5 baseline reported by [13] as figure 5.12d case 1.) The magnetic field we currently use is slightly different than either. Besides having a higher peak field strength, 300G versus 180G, which would be easily scalable, the field lines are completely different. Figure 5-5 has mostly radial field lines with lower B_{min}/B_{max} on most lines than figure 3-1. Figure 5-6 has slightly higher B_{min}/B_{max} on most lines, implying stronger bottle effects than we currently see, and puts the minimum B on the upper wall instead of 3 to 5mm away from the upper wall as in figure 3-1.

5.4 Results without Magnetic Screens

With less curvature to the field lines and simulation results available in [12], we are very interested in running the simulation with the field pictured in figure 5-5. But because Koo's field starts 10mm downstream of the anode and does not extend to the centerline of the thruster, we will have to wait until the larger field can be extrapolated or obtained from other sources. Meanwhile, in the spirit of exploration, we will run the second field, figure 5-6, that appearers to correspond to the P5's magnetic field

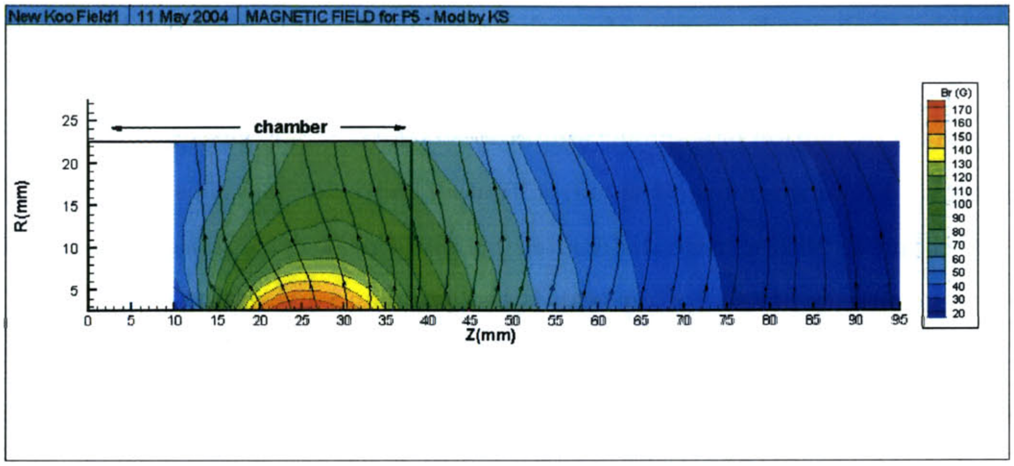

Figure 5-5: Radial Magnetic Field from Koo

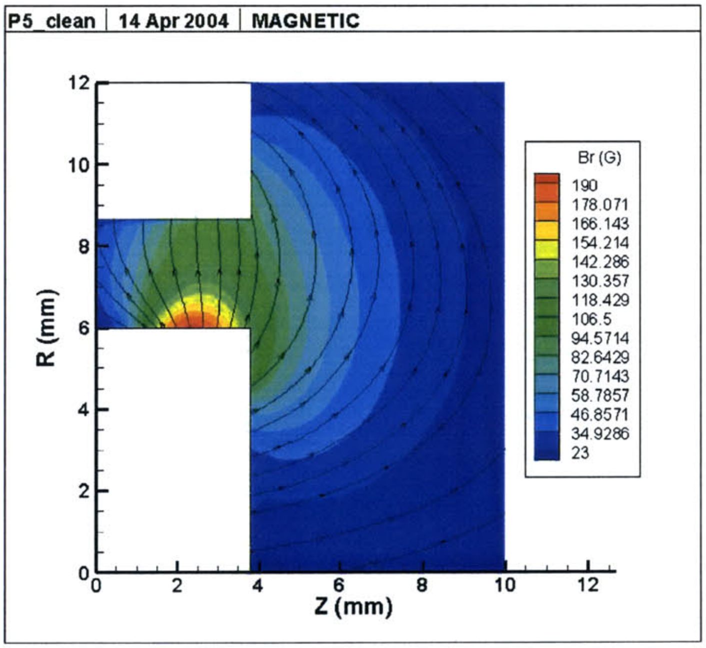

Figure 5-6: P5 Radial Magnetic Field without Magnetic Screens

without magnetic screens.

The P5 field without magnetic screens was run from a neutral filled chamber with a Hall parameter of 400 and an anode voltage of 300V. The field strength, with a peak of 190G, was unmodified. The results were very different from the old magnetic field results at the same settings. First, the startup oscillation took 1.5e-5s to peak versus 1.5e-6s for the old $\beta' = 200$ case, figure 5-7. Second, there was a strong startup oscillation, peak anode current of nearly 50A, which is missing from the old bc400 case. After the startup oscillation, the anode current appears to be heading into steady-state oscillation of a similar amplitude to the $\beta' = 400$ case, but the frequency is difficult to determine from the current data. Third, the particles more completely fill the chamber with a more distributed region of peak density, figure 5-8. Fourth, the non-negativity of the bottom wall is less pronounced resulting in a smaller area with zero sheath, figure 5-9. The peak ionization region, however, remains right next to the anode.

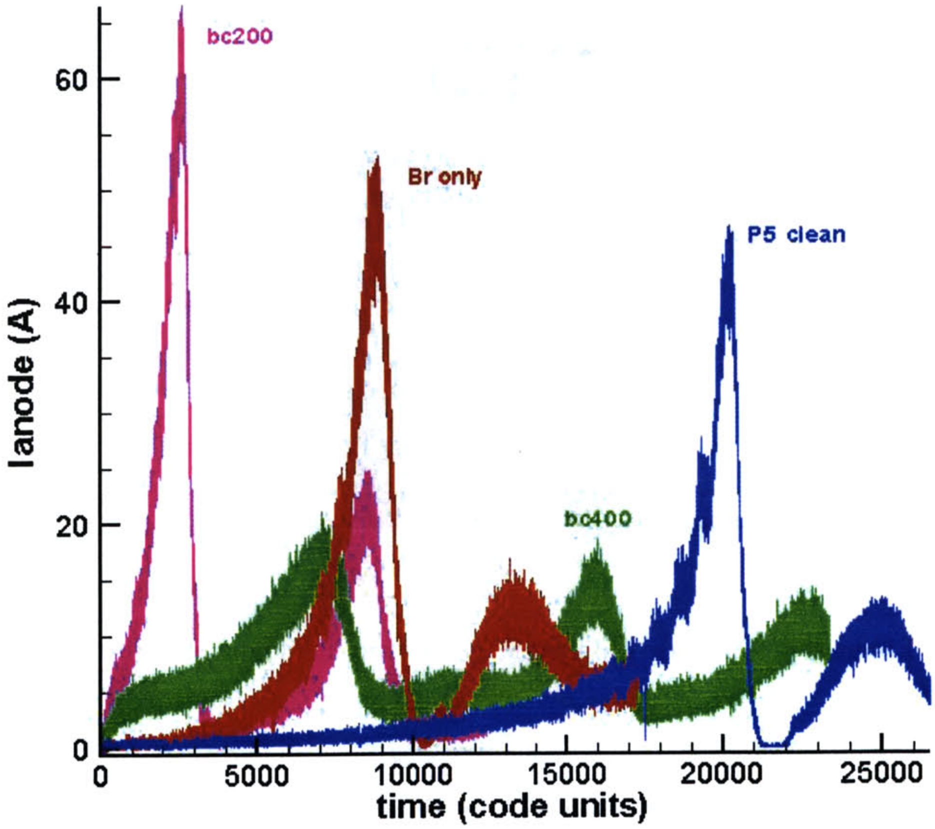

Figure 5-7: Anode Current for different magnetic field inputs. P5 clean refers to magnetic field without magnetic screens.

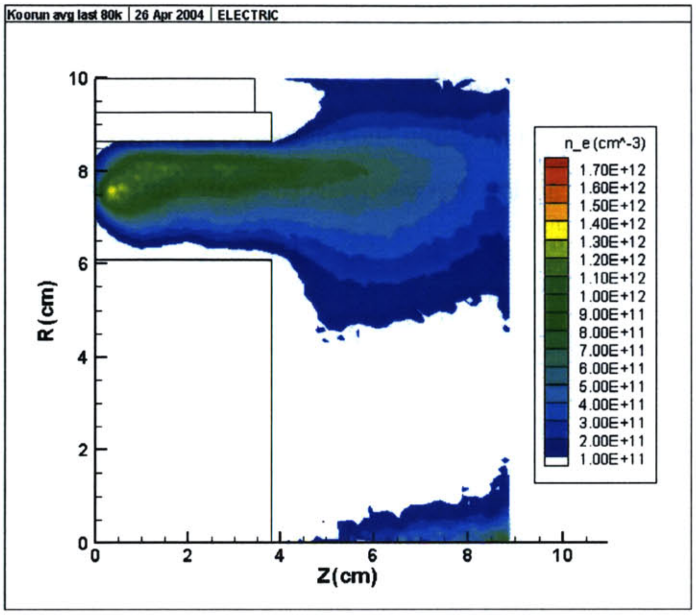

Figure 5-8: Magnetic field without magnetic screens results - average electron density

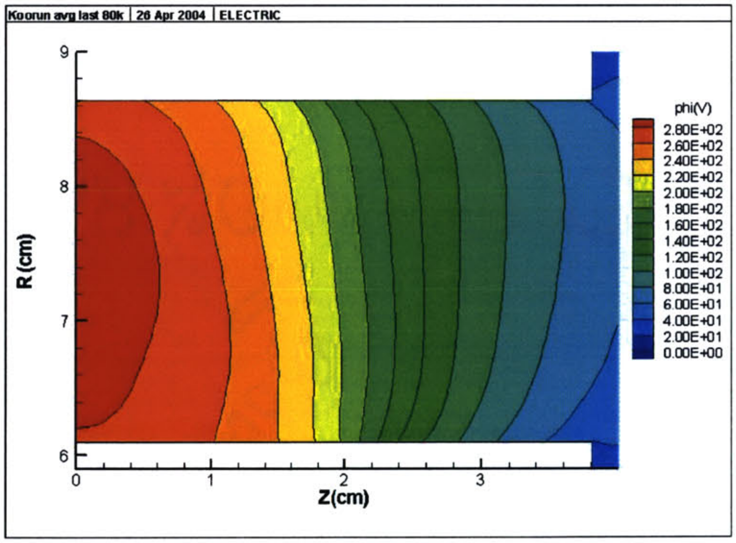

Figure 5-9: Magnetic field without magnetic screens results - average plasma potential in the chamber

5.5 Discussion

Strong magnetic mirroring is responsible for the dearth of particles in the bottom half of the chamber. The question is, why are similar strong bottling effects not seen in experimental results. Based on figure 5-5, strong mirroring should occur along the entire bottom half of the chamber. One answer would be that the velocity distributions are re-equilibrating due to collisions and cathode electrons entering the chamber. The exact effect of re-filling the angular and energy distributions is complex. An analysis of the interaction between electrostatic and electromagnetic repulsion from the walls is needed.

Chapter 6

Sputtering

6.1 Introduction

One of the main goals of this project was to make lifetime predictions for new and existing thrusters. To this end, we implemented two sputtering models. The first was a simple yield model that we used to verify the basic functions. The second was a more complex yield model based on Yamamura's [4] formulas that included a more realistic ejection angle for the sputtered neutrals.

6.2 Simple Model

In this basic yield model both the chamber walls and the inner pole piece are assumed to be pure Boron Nitride. Sputtered particles are emitted with the incident ion's energy and a random velocity direction. The sputtered particles are treated as BN neutral particles, and allowed to undergo all collisions except ionization collisions.

The sputtering yield formula is taken from [14] which concludes that for energies less than 100eV all ion-target pairs follow the relation:

$$Y_i = \frac{S_i}{U_s}(E_i - 4U_s) \tag{6.1}$$

Y_i is the sputtering yield for a particular ion-target pair, U_s is the sublimation energy of the target, E_i is the energy of the incident ion, and S_i is the sputtering yield factor which must be obtained experimentally. A sputtering yield factor S_i of 0.01 is taken from [15], who derived the sputtering coefficient from experimental data taken by [16]. The sublimation energy of Boron Nitride is estimated to be 5eV, based on the sublimation energies of Boron and Nitrogen, table 6.1.

This model is an improvement on the basic sputtering idea that at low energies the yield, the number of expelled atoms per incident ion, is proportional to the energy of the incident ion, or $Y = K(E - E_T)$. K is a constant. E is the incident ion's energy, and E_T is the threshold energy. From experiments with 117 different ion-target combinations, [14] determines the factor $4U_s$ approximates the sputtering threshold energy and $K = S_i/U_s$. This model has no angular dependance because, based on the work of [17], [14] concludes that the threshold energy has a very small angular dependance and the total yield has no angular dependance for energies less than 6 times the threshold energy or 24 times the sublimation energy. For higher energies, [14] observes angular dependencies mostly coinciding with Sigmund [18], on whose theories Yamamura's model is partially based.

6.3 Yamamura Model

A more sophisticated sputtering model uses functions taken from Cheng [5] to implement the Matsunami normal yield and Yamamura angular yield models [4]. The chamber walls and the inner pole piece are treated as 50% Boron Nitride 50% Silicon Dioxide, but because the needed coefficients are not available for this ceramic, sputtering is performed for elemental Boron, Nitrogen, Silicon, and Oxygen separately. The chemical element to be sputtered by any particular incoming ion is chosen at random, with each element having an equal probability.

6.3.1 Yamamura Normalized Angular Yield

In heavy-ion sputtering the threshold ion is dependant on incidence angle in the form

$$\frac{Y(\theta)}{Y(0)} = \cos\theta^{-f_s}[\frac{1-(E_{th}/E)^{1/2}\cos\theta}{1-(E_{th}/E)^{1/2}}] \tag{6.2}$$

The threshold energy in this case is not yet understood, therefore [4] recommends using a formula similar to light-ion sputtering

$$\frac{Y(\theta)}{Y(0)} = \cos\theta^{-f}\exp[-f\cos\theta_{opt}(\cos\theta^{-1}-1)] \tag{6.3}$$

letting the exponent f include the effect of the angular threshold energy.

$$\begin{aligned} f &= f_s(1+2.5\frac{1-\zeta}{\zeta}) \\ \zeta &= 1-(E_{th_{ang}}/E)^{\frac{1}{2}} \\ E_{th_{ang}} &= 1.5\frac{U_s}{\gamma}[1+1.38(M_1/M_2)^h]^2 \\ \gamma &= 4M_1M_2/(M_1+M_2)^2 \end{aligned}$$

The exponent h is 0.834 for light-ion sputtering, $M_2 > M_1$, and is equal to 0.18 for heavy-ion sputtering, $M_2 < M_1$. f_s, the Sigmund f, is given for many different ion-target pairs in [4] as is the angular threshold energy, $E_{th_{ang}}$.

The optimum incidence angle, θ_{opt}, is the angle which gives the maximum yield. For heavy-ion sputtering

$$\theta_{opt} = 90\deg -286.0\psi^{0.45} \tag{6.4}$$

The parameter ψ relates to surface channelling. It is a function of $\frac{1}{\sqrt{E}}$, and is tabulated in [4] for $E = 1eV$.

6.3.2 Yamamura Normal Yield

The normal yield, $Y(E)$ must be known to determine the angular yield from the above normalized formulas. [4] recommends using the third Matsunami formula

$$Y(E) = P\frac{s_n(\epsilon)}{1 + 0.35U_s s_e(\epsilon)}[1 - (E_{th_{norm}}/E)^{1/2}]^{2.8} \tag{6.5}$$

ϵ is the LSS reduced energy defined as

$$\begin{aligned} \epsilon &= E/E_L \\ E_L &= \frac{M_1 + M_2}{M_2}\frac{Z_1 Z_2 e^2}{a} \\ a &= 0.4685(\frac{1}{Z_1^{2/3} + Z_2^{2/3}})^{\frac{1}{2}} \end{aligned}$$

Z_1 and Z_2 are the atomic numbers of the incoming ion and the target material respectively. The threshold energy is this time

$$E_{th_{norm}} = U_s[1.9 + 3.8(M_1/M_2) + 0.314(M_2/M_1)^{1.24}] \tag{6.6}$$

The normal threshold energy, the parameter P, E_L, and the sublimation energy U_s are tabulated by Yamamura, table 31 in [4], but the LSS elastic stopping cross section $s_n\epsilon$ and $s_e\epsilon$ must be calculated from

$$s_e(\epsilon) = k\epsilon^{1/2} \tag{6.7}$$

$$s_n\epsilon = \frac{3.441\sqrt{\epsilon}\log(\epsilon + 2.718)}{1 + 6.355\sqrt{\epsilon} + \epsilon(-1.708 + 6.882\sqrt{\epsilon})} \tag{6.8}$$

The inelastic coefficient k is a function of the atomic numbers and masses of the ion and target, and is tabulated by [4].

6.3.3 Low Energy Approximation

When $E < E_{th}$ f goes to infinity, therefore an approximation to the yield must be made for low energies. The method employed by Cheng, is to linearly extrapolate

Table 6.1: Parameters Used in Yamamura Equations

element name	Silicon	Boron	Nitrogen	Oxygen
P	13.66	5.231	8.625	18.7
$E_L(eV)$	5.913e5	4.526e5	5.105e5	5.228e5
k	0.112	0.102	0.107	0.107
$E_{th_{norm}}(eV)$	91.16	277.3	184.6	86.04
$U_s(eV)$	4.63	5.77	4.92	2.6
f_s	1.8	1.7	1.72	1.76
$\psi(1eV)$	0.0978	0.1099	0.073	0.0845
$E_{th_{ang}}(eV)$	95.24	308	198.9	91.58
pseudoE(eV)	150.0	640.0	385.0	161.0
absE(eV)	91.3	280.0	180.0	85.0

the yield from 0 yield at the normal threshold energy to the yield at some pesudothreshold energy where the Yamamura formulation still gives reasonable results.

All the inputs to the above equations that can be precomputed as well as ψ for 1eV are listed for each target element in table 6.1.

6.3.4 Neutral Ejection Velocity

Sputtered neutrals are ejected with the incoming ion's energy and a direction based on the ion's energy and impact angle. The outgoing direction is statistically selected based on the cumulative distribution functions

$$F_1(\theta_1) = \frac{2}{1 - \epsilon\cos\theta}[\frac{1}{2}x^2 - \frac{1}{4}\epsilon\cos\theta\{x^2 + (\frac{1}{2}x^3 - x + \frac{1}{2x})\ln[\frac{1-x}{1+x}]\}] \tag{6.9}$$

and

$$F_2(\phi) = \frac{1}{2\pi}[\phi - \frac{\frac{3\pi}{8}\epsilon\sin\theta\sin\theta_1\sin\phi}{1 - \frac{1}{2}\epsilon\cos\theta\gamma(\theta_1)}] \tag{6.10}$$

where $x = \sin\theta_1$, $\epsilon = \sqrt{\frac{E_{th}}{E}}$, θ is the ion's angle perpendicular to the wall, θ_1 is exit angle perpendicular to the wall, and ϕ is the exit angle in the plane of the wall. The full derivation of these distribution functions is in [5].

6.4 Model Validation

The only experimental data we have found so far for BN and BNSiO2 sputtering by Xenon at energies near what we see in the P5 is from [16]. [16] presents data from a 350eV, 500eV, and 1000eV ion source. These ion energies are still several times higher than what we expect to hit the wall in the simulation due to inefficiencies and a weak sheath.

The simple model is compared to [16]'s data by directly calculating the yield in Matlab at 350V, 500V, and 1000V. The results are shown in figure 6-1. The simple model over predicts the yield by a factor of 6. Note that the simple model is designed for energies less than 100eV, and its angular independence is not valid for energies greater than 120eV (6 times the threshold energy $6 \times 4U_s = 6 \times 4 \times 5 = 120eV$), therefore this comparison may not be fair. It may be that we are still under predicting the threshold energy, or that the sputtering yield coefficient is incorrect. Either way, our confidence in the simple model is low. With more tweaking to match experimental data, reducing the sublimation energy to 20eV (threshold energy of 80eV) for example, the simple model could be a quick way of getting an estimate of the total yield averaged over all angles. With the more accurate Yamamura model already implemented, however, there seems little reason to continue with the simple model.

The Yamamura model is compared to [16]'s data by building a test harness around Cheng's C functions. Ions at 10 through 700eV over angles 0 to 90 degrees are fed to the model. The results, shown in figure 6-2, are a bit more difficult to interpret because the Yamamura model calculates the yield for each element in the wall material while [16] tests the BN, SiO_2, and $BNSiO_2$ compounds.

One failure of the Yamamura implementation comes from having to sputter each element separately. [16] finds that BN is preferentially sputtered, even though it has a lower yield separately, and controlls the overall yield of the BNSiO2 ceramic. We choose the sputtered element randomly before calculating the yield, therefore the total yield is just the average of the elemental yields. Figure 6-3 shows the supposed

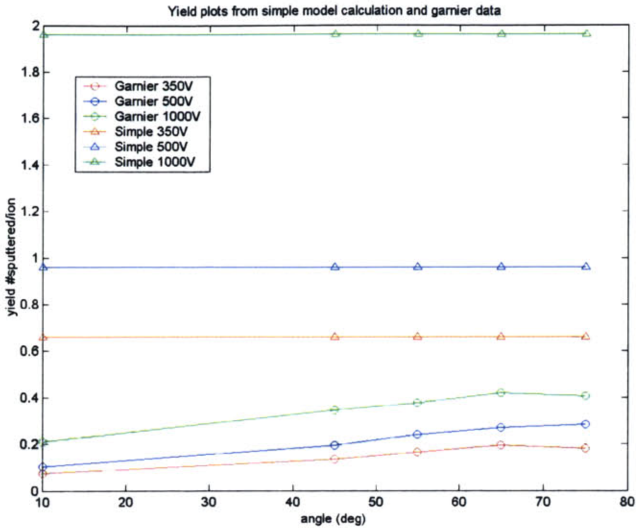

Figure 6-1: Yield Curve for Simple Sputtering Model

BN, SiO_2, and $BNSiO_2$ yields along with the [16] data. The Yamamura model results are very close to the experimental data at angles near normal incidence, and over predict the yield by only a factor of 7 at the peak. The Yamamura results and [16]'s data both show the same trend with impact angle with maximum yield between 60° and 70° from normal.

6.5 Full Simulation Sputtering Results

Both the simple and Yamamura models were run at anode voltages of 300 and 500 for 8 to 10 thousand iterations, or 4.4e-7s of simulated time. The Yamamura model was also run at 700V. Other than the addition of sputtering, simulation settings were the same as reported for the 3kW and 5kW runs in chapter 3. The runs were started from the end of the 3kw startup plasma oscillation.

In 4.4e-7s there were at least 15,000 ion impacts at 3kW and at least 20,000 ion impacts at 5kw, mostly along the top wall in both cases. No sputtered neutrals were reported for either model at 3kW. At 5kW, only 1 sputtered neutral was reported for 23,981 ion impacts with the Yamamura model, and 3 sputtered neutrals were reported for 27,297 ion impacts with the simple model. This corresponded to a yield of 4.16997e-05 and 1.10e-04 sputtered particles per ion respectively. The final Yamamura run, at 700V anode voltage, saw 34,535 ion impacts and 8 sputtered neutrals for a yield of 2.32e-04. The simulated yields are plotted along with selected predicted yields from the above section, figure 6-4.

6.6 Discussion

In our brief tests so far, all that can be said is that most ions are below threshold for either model at 3kw, 5kw, and 7kw settings. Longer runs are needed to fully evaluate the models, particularly the velocity at which sputtered neutrals are ejected. It may be beneficial to adjust the absolute threshold energies used by the Yamamura model. At the low energies we seem to be observing, small changes in threshold energies can results in large changes in yield. In addition, the weak sheath is reducing the incoming ion energy and angle, $\Delta V_{sh} \sim T_e$ instead of $5T_e$, and a correction in the code should be implemented. A record of the actual ion incident angles and energies should also be added for model evaluation and thruster design purposes.

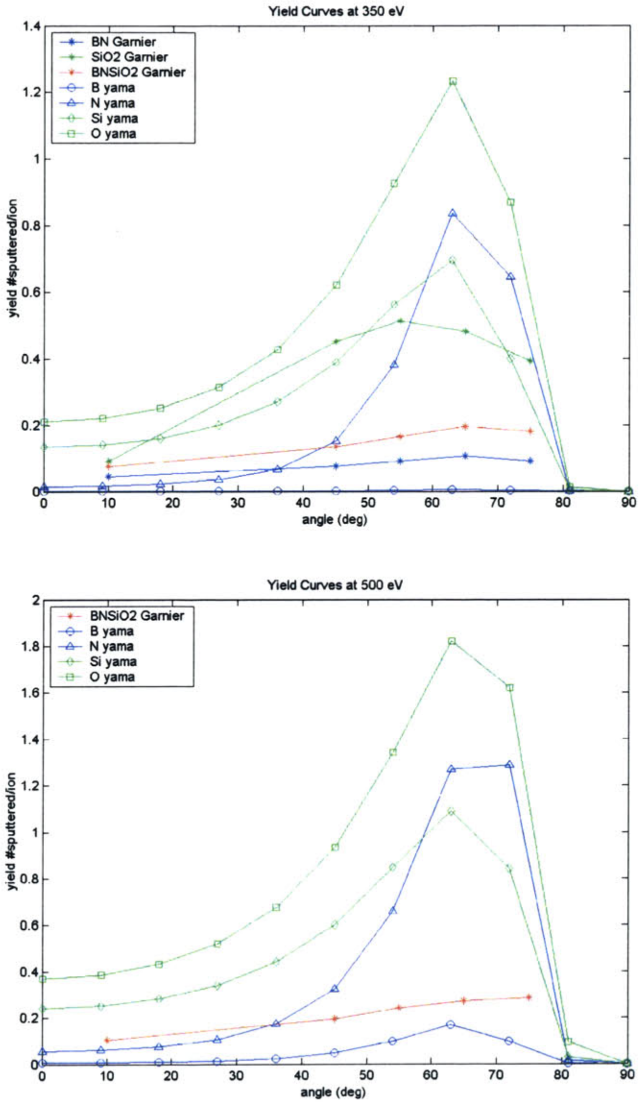

Figure 6-2: Yamamura Model Elemental Results Compared to Garnier Data 350V (top) 500V (bottom)

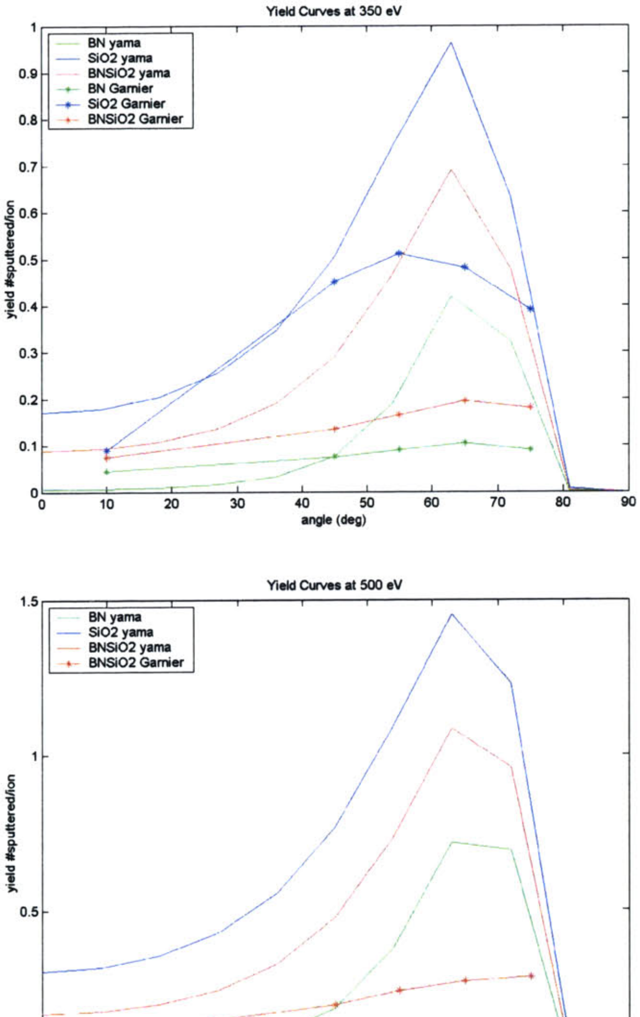

Figure 6-3: Yamamura Model Compound Results Compared to Garnier Data 350V (top) 500V (bottom)

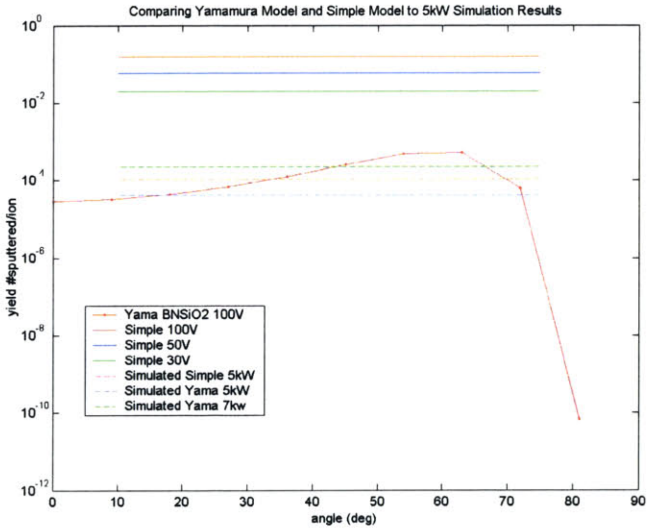

Figure 6-4: Comparing Yamamura and Simple Model to Simulated Yields

Chapter 7

Conclusions and Future Work

We successfully simulated the P5 at 3kw and 5kw operating conditions. While the simulation results showed a few deviations from the probe data reported by [3], particularly in the placement of peak densities, we are confident that the basic physical models in the simulation, (particle motion, collisions, transport, Poisson solver), are correct. The major questions remaining are why must we use such a large Hall parameter, 200 to 400 instead of the classical value of 16, and why is the peak ionization near the anode instead of the axial location of maximum magnetic field.

Testing the electron transport mechanisms from several angles confirmed that the simulated electron mobility agreed with the theoretical mobility based on the simulated collision frequencies. Secondary electron emission from the walls had a strong effect on electron transport apparently by increasing the number of electrons capable of ionizing and hence the ionization and excitation rates in the simulation. While total mobility remained nearly constant when SEE was removed, the relative contributions of classical collisions, anomalous collisions, and wall effects changed.

Magnetic mirroring was discovered to have a stronger effect on the simulation than what had been reported experimentally. Further testing is needed to determine why. The mirroring appeared to be independent of the electron transport question, although the collisions and wall effects that produce mobility also influence the observed velocity distribution functions.

7.1 Future Work

Suggestions for further study are

- Conduct straight field mobility testing with varying Hall Parameter. Check that the total collisions/mobility decreases with increasing Hall Parameter in the full simulation. Currently we observe increasing classical collision rates with increasing Hall Parameter. Classical Collision rates should be independent of Hall Parameter.

- Run the full simulation and "straight" magnetic field with the logical sheath off. The logical sheath was never fully tested. After a bit more thinking, and particularly in light of the SEE findings, we do not believe the electron energy loss needs correcting. Electron energy loss to the walls is $\Gamma_{eW} = \Gamma_e 2kT_e$ where $\Gamma_e = \frac{n_e \bar{c}_e}{4} e^{-\frac{e\Delta\phi}{kT}}$ is the electron number flux to the sheath. While Γ_e is elevated due to the smaller sheath strength ϕ, all other energy loss/gain mechanisms, i.e. ionization collisions, motion up the potential well to the anode, are accelerated by the same factor $\sqrt{f}$, therefore the electron temperature should remain constant with varying mass factor without any extra intervention in the code.

- Obtain electron velocity distribution functions paying particular attention to ratio of perpendicular and parallel components for mirroring. To explain the strong effect of magnetic mirroring in our simulations, which is not seen in experiment, we should determine
  - How similar are the mean time between randomizing collisions and the time to travel between channel walls?
  - Do the velocity distributions "refill" in both energy and angle?
  - If so what is the dominant factor in reintroducing high $v_{||}$ electrons to the simulation? New cathode electrons? Collisions?

  - Examine effect of secondary electron emission from the walls on the electron velocity distribution functions. In the no SEE runs presented here, particles appeared to fill the chamber more completely.

- Perform high power runs.

- Implement a correction on the ion energy hitting the wall due to the weakened sheath. Test the Yamamura sputtering model in longer runs and at higher power. If the sputtering yield is still very low, investigate adjusting the threshold conditions. Compare results to erosion measurements from other SPT Hall thrusters, for example [19] or [20].

- Explore different cathode conditions. The energy at which electrons are injected to the free space boundary was never fully tested. The cathode could be included in the simulation region by assuming a 12-o-clock position azimuthaly and placing the cathode at the top of the grid, or by assuming a center core cathode. Busek has high power thrusters with a center cathode, from where experimental data could be obtained for comparison.

- Check free space and centerline collisions for bugs.

- Remove obsolete functions and thoroughly debug the software. This may have to wait until the parallel code is running reliably. The code is currently too messy to be tested by direct reading, and too slow to make careful incremental testing practical.

- Investigate recent diffusion work by Cappelli [21], which suggests different diffusion rates in the chamber and plume. While we have already observed the interplay of classical and anomalous collisions in different regions of the simulation, Cappelli's work may shed light on our choice of Hall parameter.

- Implement an accommodation coefficient other than 1 for neutrals at the wall.

Bibliography

[1] James J. Szabo. *Fully Kinetic Numerical Modeling of a Plasma Thruster.* PhD thesis, MIT, 2001.

[2] Vincent Blateau. PIC simulation of a ceramic-lined Hall-effect thruster. Master's thesis, MIT, 2002.

[3] James Matthew Haas. *Low-Perturbation Interrogation of the Internal and Near-Field Plasma Structure of a Hall Thruster Using a High-Speed Probe Positioning System.* PhD thesis, University of Michigan, 2001.

[4] Y. Yamamura, Y. Itikawa, and N. Itoh. Angular dependence of sputtering yields of monatomic solids. *Institute of Plasma Physics*, June 1983. IPPJ-AM-26.

[5] Shannon Cheng. Computational modeling of a Hall thruster plasma plume in a vacuum tank. Master's thesis, MIT, 2002.

[6] Vincent Blateau, Manuel Martinez-Sanchez, and Oleg Batishchev. A computational study of internal physical effects in a Hall thruster. In *Joint Propulsion Conference*, Indianapolis, Indiana, July 2002. AIAA-2002-4105.

[7] Frank Stanley Gulczinski. *Examination of the Structure and Evolution of Ion Energy Properties of a 5kW Class Laboratory Hall Effect Thruster at Various Operational Conditions.* PhD thesis, University of Michigan, 1999.

[8] Kay Sullivan, Manuel Martinez-Sanchez, Oleg Batishchev, and James Szabo. Progress on particle simulation of ceramic-wall Hall thrusters. In *International*

Electric Propulsion Conference, number 28, Toulouse, France, 2003. IEPC-03-278.

[9] E. Ahedo, J.M. Gallardo, and Manuel Martinez-Sanchez. A model of the hall thruster discharge with the effects of the interaction with the lateral walls.

[10] Oleg Batishchev and Manuel Martinez-Sanchez. Charged particles transport in the hall effect thruster. In *International Electric Propulsion Conference*, number 28, Toulouse, France, 2003. IEPC-03-188.

[11] E. Ahedo, P. Martinez Cerezo, and Manuel Martinez-Sanchez. Model of plasma-wall interaction effects in a hall thruster. In *Joint Propulsion Conference*, Salt Lake City, Utah, July 2001. AIAA-2001-3323.

[12] Justin W. Koo and Ian D Boyd. Computational modeling of stationary plasma thrusters. In *Joint Propulsion Conference*, Huntsville, AL, July 2003. AIAA-2003-10113.

[13] Richard Robert Hofer. *Development and characterization of High-Efficiency, High-Specific Impulse Xenon Hall Thrusters*. PhD thesis, University of Michigan, 2004.

[14] Michael J. Barlow. The destruction and growth of dust grains in interstellar space. *Monthly Notes of the Royal Astronomical Society*, 183:367–395, 1978.

[15] Subrata Roy and B.P. Pandey. Modeling the effect of plasma-wall interaction in a Hall thruster. In *Aerospace Sciences Meeting and Exhibit*, number 41, Reno, NV, 2003. AIAA. AIAA-2003-0493.

[16] Y. Garnier, V. Viel, J.-F. Roussel, D. Pagnon, L. Magne, and M. Touzeau. Investigation of Xenon ion sputtering of one ceramic material used in SPT discharge chamber. In *International Electric Propulsion Conference*, number 26, Kitakyushu, Japan, 1999. IEPC-99-083.

[17] J.F. Cuderman and J. J. Brady. *Surface Science*, 10:410, 1968.

[18] Peter Sigmund. Theory of sputtering. i. sputtering yield of amorphous and polycrystalline targets. *Physical Review*, 184:383–416, 1969.

[19] Peter Y. Peterson and David H. Manzella. Investigation of the erosion characteristics of a laboratory Hall thruster. In *Joint Propulsion Conference*, Huntsville, AL, July 2003. AIAA-2003-5005.

[20] Vladimir Kim, Vyacheslav Kozlov, Alexander Semenov, and Igor Shkarban. Investigation of the Boron Nitride based ceramics sputtering yield under its bombardment by Xe and kr ions. In *International Electric Propulsion Conference*, number 27, Pasadena, CA, 2001. IEPC-01-073.

[21] M. A. Cappelli, N.B. Meezan, and N. Gascon. Transport physics in Hall plasma thrsuters. In *Aerospace Sciences Meeting and Exhibit*, number 40, Reno, NV, 2002. AIAA. AIAA-2002-0485.

Appendix A

Effect of SEE on Classical Collisions

While we do not have an accurate report of the total collision frequency executed in the code, we do have an output file that claims to report, in unknown units, the three ionization frequencies and the excitation collision frequency. If these data can be trusted, what we notice is a significant increase in the classical collision frequencies when SEE is reduced. The doubling of the estimated classical mobility in the chamber, table 4.2, when secondary electron emission is turned off supports this finding. Figures A-1, A-2, A-3, A-4 illustrate the relative number of ionization and excitation collisions occurring with and without secondary electron emission with a Hall Parameter of 200. All reported frequencies more than double when SEE is removed.

In retrospect, the reason behind the increased ionization is straight forward. Logically, reducing SEE has the same effect on electron losses to the walls as increasing the sheath strength. Assuming the ion flux to the wall is unaffected, no SEE reduces the positive charge accumulation on the wall resulting in fewer electrons necessary to reach equilibrium. This in turn results in more high energy electrons available for other processes like ionization.

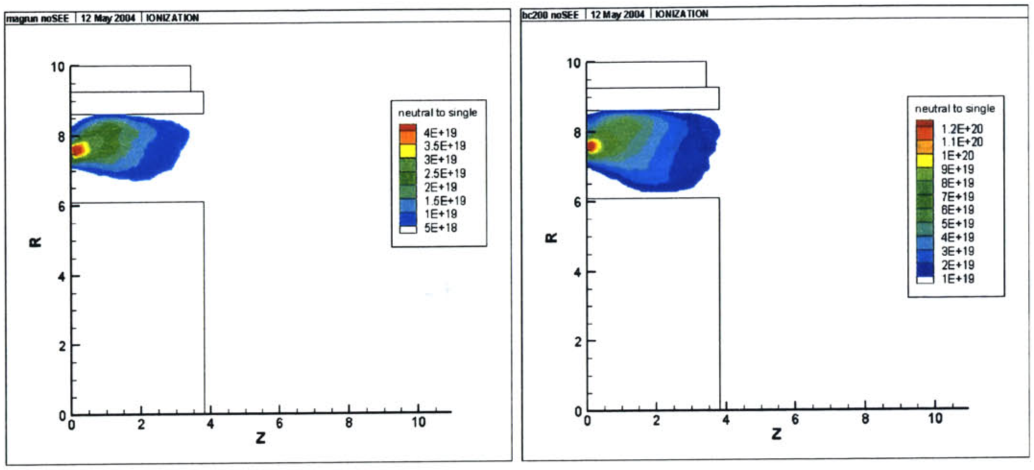

Figure A-1: Neutral to Single Ionization Rate with $\beta' = 200$(left)$\beta' = 200$ noSEE (right)

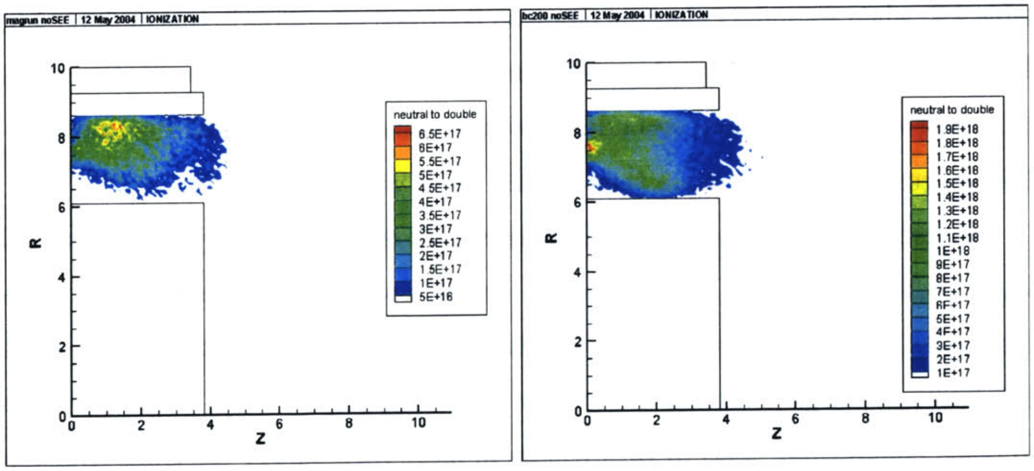

Figure A-2: Neutral to Double Ionization Rate with $\beta' = 200$(left)$\beta' = 200$ noSEE (right)

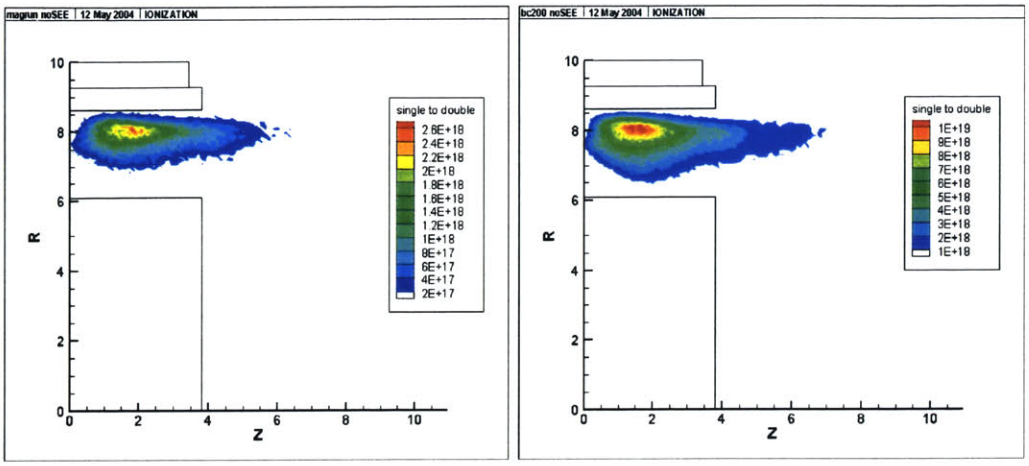

Figure A-3: Single to Double Ionization Rate with $\beta' = 200$(left)$\beta' = 200$ noSEE (right)

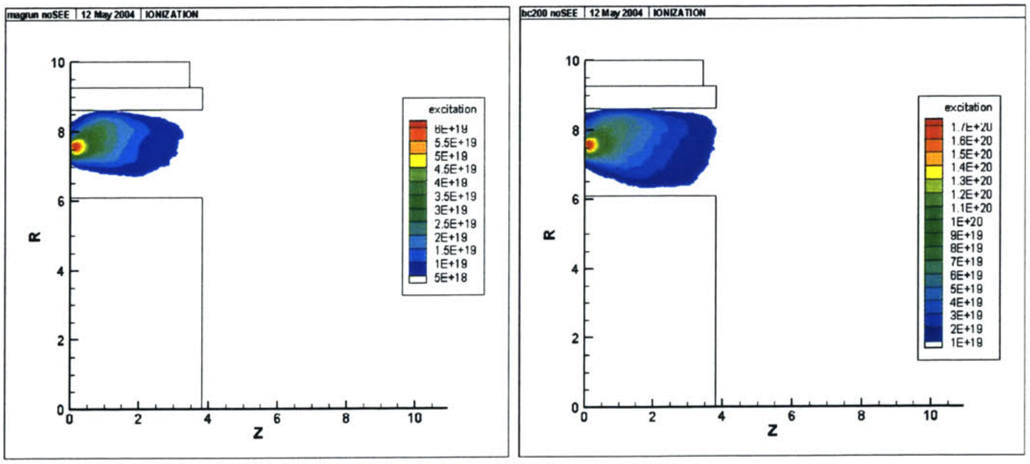

Figure A-4: Excitation Rate with $\beta' = 200$(left)$\beta' = 200$ noSEE (right)